Available online at www.sciencedirect.com
ScienceDirect
Precambrian Research 161 (2008) 317–340
Precambrian Research
www.elsevier.com/locate/precamres

Evidence for HFSE and REE mobility during calc-silicate metasomatism, Mesoarchean (~3075 Ma) Ivisaartoq greenstone belt, southern West Greenland

J.C. Ordóñez-Calderón [a,*], A. Polat [a], B.J. Fryer [a,b], J.E. Gagnon [a,b], J.G. Raith [c], P.W.U. Appel [d]

[a] *Department of Earth and Environmental Sciences, University of Windsor, Windsor, Ont., Canada N9B 3P4*
[b] *Great Lakes Institute for Environmental Research, University of Windsor, Windsor, Ont., Canada N9B 3P4*
[c] *Department of Applied Geosciences and Geophysics, University of Leoben, Leoben A-8700, Austria*
[d] *Geological Survey of Denmark and Greenland, 1350 Copenhagen, Denmark*

Received 7 February 2007; received in revised form 31 August 2007; accepted 3 September 2007

Abstract

The Mesoarchean (*ca.* 3075 Ma) Ivisaartoq greenstone belt consists dominantly of variably deformed and metamorphosed mafic to ultramafic flows (basalts to picrites). In addition, there are minor serpentinites, gabbros, clinopyroxene-rich cumulates, and volcaniclastic and siliciclastic sedimentary rocks. Primary volcanic structures such as pillows and volcanic breccia are well preserved in low strained zones. The belt underwent intense metasomatic hydrothermal alteration between 3075 and 2961 Ma. An early stage of calc-silicate metasomatism (stage-I) resulted in the formation of epidosites in pillow cores, pillow interstitials, and intrusive margins of gabbroic dykes. This alteration appears to have resulted from sea-floor hydrothermal alteration. A second stage of calc-silicate metasomatism (stage-II) formed centimeter- to meter-scale layers concordant to discordant relative to the regional foliation. These layers consist of diopside + garnet + epidote + plagioclase + quartz + titanite ± vesuvianite ± calcite ± actinolite ± scheelite. The second stage calc-silicate rocks are associated with shear zones and their origin is attributed to interaction of reactive fluids with mafic and ultramafic rocks during regional metamorphism.

Both stages of calc-silicate metasomatism caused significant mobilization of major elements (Si, Mg, Ca, Fe, Na, K, and Mn), LILE (Rb, Cs, Sr, Ba, Pb), and LREE. Heavy rare earth elements (HREE) and HFSE (Th, Nb, Ta, Zr, Ti) remained relatively immobile during stage-I metasomatic alteration but were variably disturbed during the stage-II metasomatism. Accordingly, the stage-II calc-silicate rocks exhibit evidence for significant mobility of Th, Nb, and Ta on a local scale (1–4 m), whereas Zr and Ti were not significantly mobilized. This resulted in calc-silicates with complementary trace element patterns displaying extreme negative to positive Nb-anomalies ($Nb/Nb^* = 0.19–7.28$). Transition metals Ni, V, Co, Cr, and Sc were relatively immobile during both metasomatic events.

Amphibolites spatially related to the second stage calc-silicate rocks preserve mineralogical and major element characteristics consistent with a mafic to ultramafic composition. However, their near-primary magmatic trace element compositions were variably modified due to strong REE mobility during the stage-II metasomatic event. This gave rise to various REE characteristics including LREE-enriched, LREE-depleted, and U-shape REE patterns. Some of these element patterns resemble those shown by modern boninites and mid-ocean ridge basalts (N-MORB). In contrast, the least altered amphibolites exhibit similar trace element patterns to those displayed by the least deformed non-metasomatized mafic and ultramafic pillow flows. They possess relatively flat trace element patterns with negative Nb–Ta anomalies indicating a subduction zone geochemical signature.

Keywords: Archean; Greenstone belt; Pillow basalt; Calc-silicate; Metasomatism; Element mobility

1. Introduction

Many Archean greenstone belts display geochemical and petrographic evidence for post-magmatic alteration resulting from fluid-rock interaction during sea-floor, regional, and

* Corresponding author. Tel.: +1 519 253 3000x2486.
E-mail address: ordonez@uwindsor.ca (J.C. Ordóñez-Calderón).

0301-9268/$ – see front matter © 2007 Elsevier B.V. All rights reserved.
doi:10.1016/j.precamres.2007.09.004

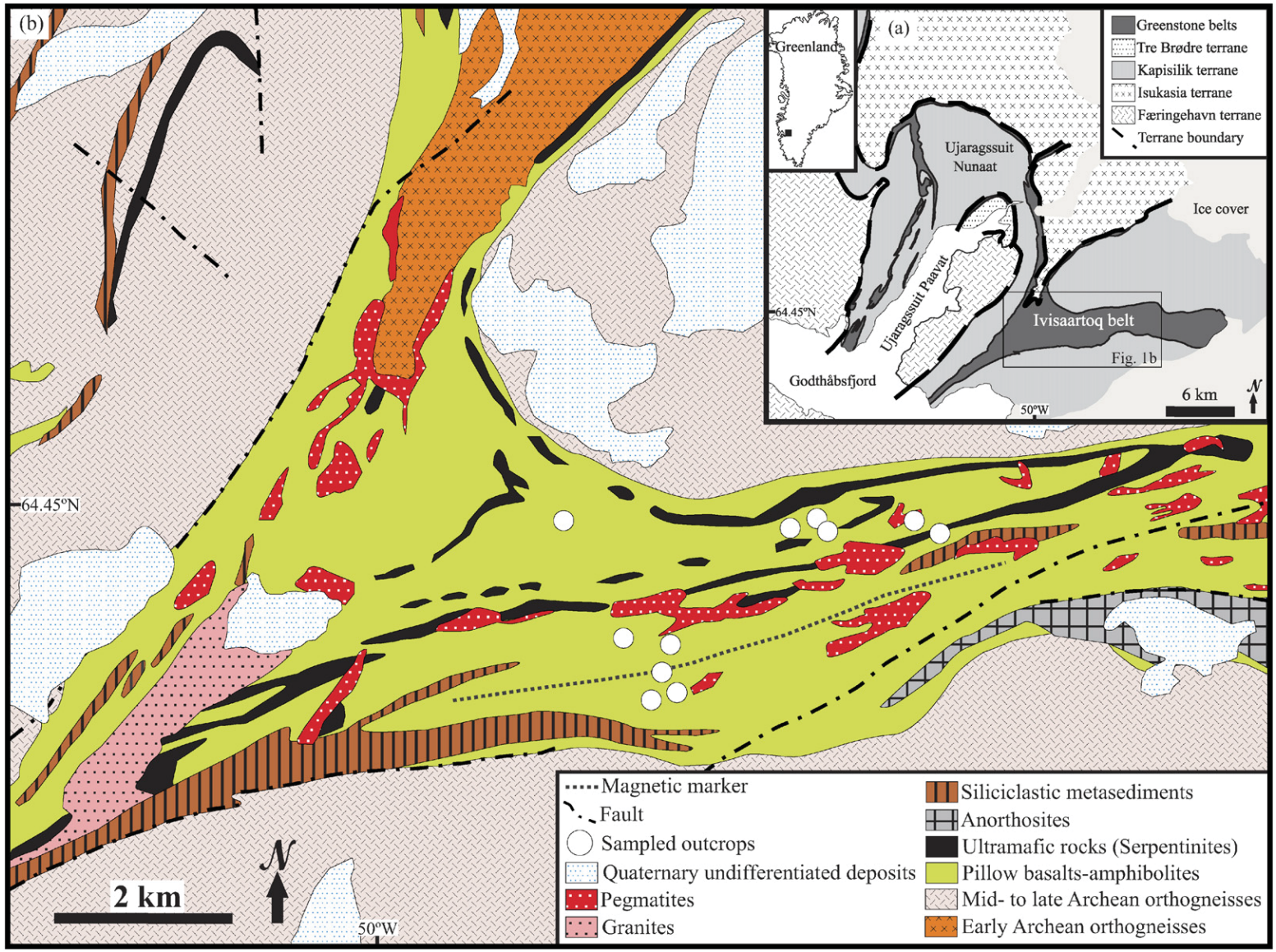

Fig. 1. (a) Early to late Archean tectonic terranes map of the northeastern Nuuk region (modified after Friend and Nutman, 2005). (b) Geological map of central Ivisaartoq belt and surrounding areas (modified from Chadwick and Coe, 1988).

contact metamorphism (Fryer et al., 1979; Gruau et al., 1992, 1996; Lahaye et al., 1995; Polat et al., 2003; Terabayashi et al., 2003; Weiershäuser and Spooner, 2005). Alteration processes in the Archean appear to have significantly modified the primary igneous textures and geochemical signatures of greenstone belts. Post-depositional alteration generally results in the mobility of most major elements and LILE (e.g., K, Sr, Rb, Cs, Ba, Pb), whereas the abundances of the REE (La–Lu), HFSE (e.g., Zr, Hf, Nb, Ta, Ti, Y), and transition metals (e.g., Ni, Cr, Co, V, Sc) are not significantly changed (Gélinas et al., 1982; Ludden et al., 1982; Middelburg et al., 1988; Polat and Hofmann, 2003). Therefore, most Archean metavolcanic rocks appear to have preserved only near-primary REE, HFSE, and transition metal geochemical compositions.

Systematic investigation of chemical changes occurring at different stages of post-magmatic alteration is important to understand the origin and geodynamic evolution of Archean greenstone belts. However, resolving post-magmatic alteration events is sometimes hindered by multiple episodes of deformation, metamorphism, and plutonism that invariably affected greenstone belts.

Despite amphibolite-facies metamorphism and polyphase deformation (Hall and Friend, 1979; Chadwick, 1985, 1990; Friend and Nutman, 2005), the Ivisaartoq belt exhibits well preserved field relationships allowing the recognition of at least two successive stages of calc-silicate metasomatism. An early metasomatic event (stage-I) occurred during sea-floor hydrothermal alteration and was followed by intense metasomatism (stage-II) coeval with the regional dynamothermal metamorphism (Polat et al., 2007a). The stage-I metasomatism is best recorded in pillow cores and rims, displaying a metasomatic zonation decreasing in intensity towards the pillow rims. The stage-II calc-silicate metasomatism is best recorded in concordant to discordant boudinaged calc-silicate layers preferentially located along shear zones.

The occurrence of non-metasomatized versus concentrically zoned pillow basalts, and their highly deformed counterparts (mafic amphibolites) variably affected by the stage-II calc-silicate alteration provides a unique opportunity to evaluate the geochemical effects associated with the different stages of post-magmatic alteration. The effects of the stage-I metasomatism on the primary geochemical characteristics of mafic and ultramafic rocks of the Ivisaartoq belt were investigated by Polat et al. (2007a). However, the geochemical changes resulting from the subsequent stage-II metasomatism and its effects on the near-primary magmatic composition of Ivisaartoq volcanic rocks are unknown. Accordingly, we present new field, petrographic, and geochemical data from the second stage metasomatic rocks and associated mafic and ultramafic amphibolites to understand the chemical and mineralogical changes that occurred during this alteration event. We report new, high precision major and trace element data for a total of 40 samples (25 amphibolites, and 15 calc-silicate rocks) to asses the effects of stage-II metasomatism on element mobility. The data presented in this study provide new insights into the geochemical effects of post-magmatic alteration on mafic to ultramafic rocks of the Ivisaartoq greenstone belt and their implications on the petrogenetic and geodynamic evolution of the belt.

2. Regional geology and field characteristics

The Ivisaartoq greenstone belt is one of the largest and best preserved Archean greenstone belts in the Nuuk region, SW Greenland (Fig. 1). This belt forms an asymmetric syncline approximately 30 km long and 1–5 km wide. Structural and geochronological studies have shown that the Nuuk region is formed by several tectonostratigraphic terranes ranging in age from 2860 to 3870 Ma (Friend et al., 1987, 1988, 1996; Nutman et al., 1989, 1993; Friend and Nutman, 2005; Garde, 2007). The Ivisaartoq belt is located within the *ca*. 3075–2960 Ma Kapisilik terrane and has an average U–Pb zircon age of ~3075 Ma (Friend and Nutman, 2005; Polat et al., 2007a). The minimum age of the belt is indicated by 2963 ± 12 Ma old granites intruding the belt (Friend and Nutman, 2005).

The Ivisaartoq belt is composed primarily of mafic and ultramafic amphibolites with minor intercalations of paragneisses, pelitic schists, quartzites, and ultramafic schists with relict olivine (Fig. 2). These rocks are the result of intense deformation and amphibolite-facies metamorphism of basalts, picrites, gabbros, diorites, siliciclastic sedimentary rocks, sulphide-bearing siliceous volcaniclastic (?) rocks, and ultramafic cumulates (Hall, 1980; Brewer et al., 1984; Chadwick, 1985, 1986, 1990; Polat et al., 2007a). Despite deformation and metamorphism,

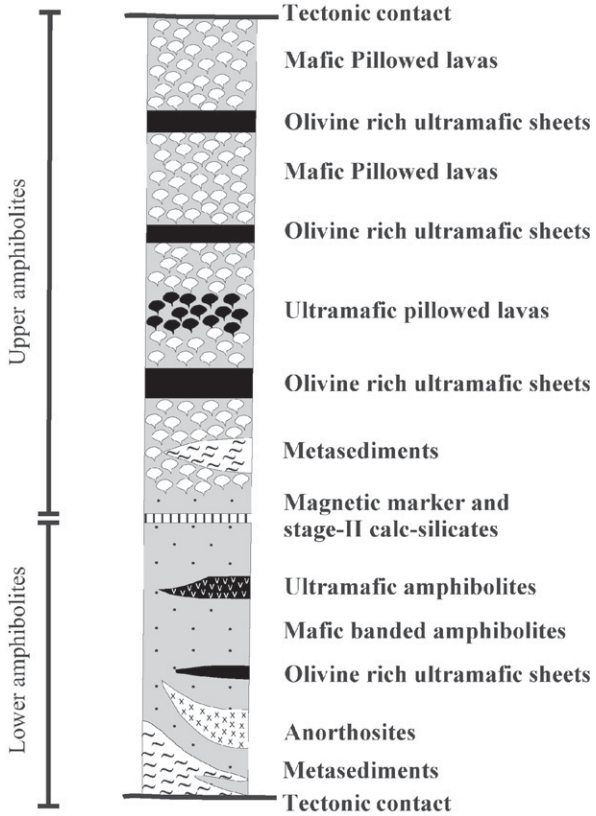

Fig. 2. Simplified stratigraphic column of the Ivisaartoq greenstone belt (modified after Chadwick, 1990).

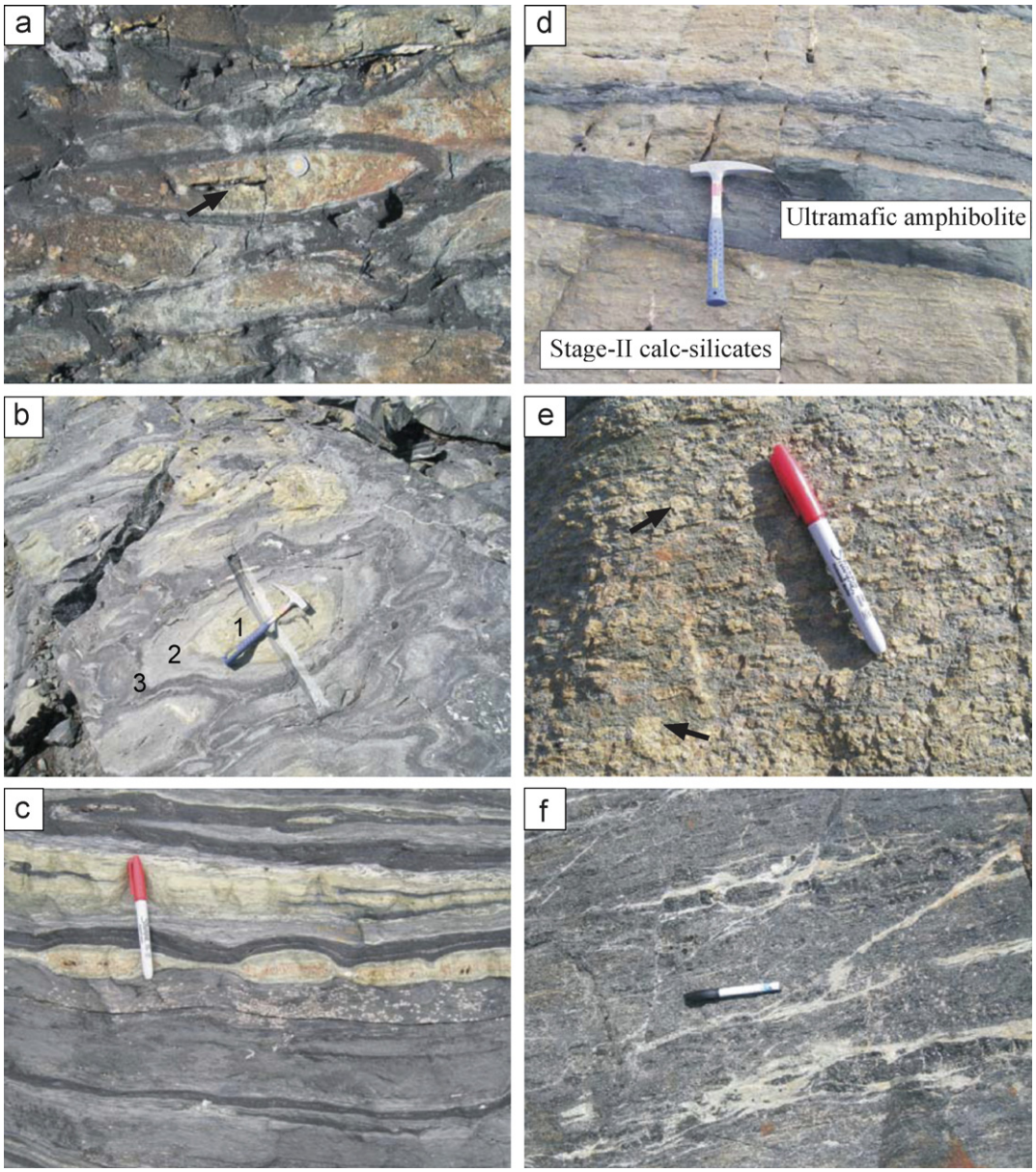

Fig. 3. Field photographs of outcrops from the Ivisaartoq greenstone belt. (a) Pillowed lavas with well preserved drainage cavities (arrow), epidosite cores (stage-I metasomatism), and pillow rims. (b) Concentrically zoned pillow lava displaying epidote-rich inner pillow core (1), calc-silicate free outer pillow core (2), and amphibole-rich pillow rim (3). (c) Boudins of stage-II calc-silicate rocks. (d) Relict ultramafic enclave in a thick layer of epidote + diopside (assemblage IIa). (e) Coarse-grained epidote-rich assemblage IIc (arrows) partially replacing the assemblage IIa. (f) Brittle discordant veins of epidote (assemblage IIc) crosscutting mafic amphibolites.

primary magmatic features such as pillow flows, concentric cooling-cracks and drainage cavities in pillows (Fig. 3(a and b)), volcanic breccia, ocelli structures in basalts, magmatic layering, and cumulate textures are well preserved in low-strain zones.

Chadwick (1990) subdivided the belt into upper and lower amphibolite groups (Fig. 2). Primary magmatic features are well preserved in the upper group. In contrast, the lower group is more deformed, and most of the primary magmatic features have been obliterated. These lithotectonic groups are bounded by an ENE-trending alteration zone approximately 50 m thick and ~10 km long. A nearly continuous thin (~10 m thick) sheet of magnetite-rich ultramafic amphibolite, called the magnetic marker, occurs within this zone and has been used as a lithologic marker separating the upper and lower groups (Chadwick, 1985, 1990). Deformation in mafic and ultramafic rocks of the upper amphibolite group increases towards the magnetic marker. Therefore, mafic and ultramafic amphibolites around the contact zone are the highly strained counterparts of the less-deformed basaltic and picritic pillowed lavas occurring higher up in the sequence. These structural characteristics suggest that major deformation was accommodated at the contact between the lower and the upper groups. This zone has been interpreted as a tectonic contact (Polat et al., 2007a).

The stage-I calc-silicate alteration overprints mineral assemblages in pillow cores, pillow interstitials, and contacts between

Table 1
Sequence of metasomatic assemblages of the stage-II calc-silicate rocks

Assemblage	Mineralogy	Characteristics
Prograde assemblage IIa	Epidote + clinozoisite + clinopyroxene + quartz + plagioclase + titanite ± apatite	Pervasive alteration replacing mafic and ultramafic metavolcanic rocks. Occur as concordant boudinaged layers (Figs. 3(c and d) and 5(a))
Prograde assemblage IIb	Garnet + clinopyroxene + titanite ± vesuvianite ± Scheelite	Coarse-grained assemblages overprinting the metasomatic assemblage IIa and stage-I calc-silicate rocks (Fig. 5(b))
Retrograde assemblage IIc	Epidote + quartz ± tremolite ± calcite	Occur as patchy alterations replacing the prograde assemblages IIa and IIb, and as brittle irregular veins transecting the amphibolites and stage-I calc-silicate rocks (Figs. 3(e and f) and 5(c–f))

pillows and gabbros (Fig. 3(a and b)). This alteration is well exposed in the upper amphibolite group. Metasomatized pillow basalts exhibit concentric structure with distinct mineralogical and chemical composition (Fig. 3(a and b)). From core to rim these include (1) empty or quartz-filled drainage cavities, (2) calc-silicate rich (diopside ± epidote ± scapolite) inner pillow cores, (3) calc-silicate free outer pillow cores, and (4) amphibole-rich pillow rims (metamorphosed chilled margins). Outer pillow cores preserve near-primary basaltic composition (Polat et al., 2007a). This concentric mineralogical and chemical zonation (Fig. 3(b)) appears to have resulted from circulation of hydrothermal fluids through drainage cavities during the early stage of sea-floor alteration predating the regional metamorphism and deformation (Appel, 1994, 1997; Raith et al., 2006; Polat et al., 2007a).

The stage-II calc-silicate rocks exhibit mineral assemblages indicating prograde (assemblages IIa, IIb) to retrograde (assemblage IIc) metamorphic conditions (Table 1). Prograde calc-silicates occur as centimeter- to meter-scale boudinaged layers and are concordant to the regional foliation (Fig. 3(c and d)). They contain relict enclaves of amphibolites up to 1 m long and 0.5 m wide (Fig. 3(d)). Retrograde calc-silicates occur as brittle veins crosscutting the regional foliation and as patchy alterations overprinting the prograde assemblages (Fig. 3(e and f)). The stage-II calc-silicate rocks are associated with shear zones and are dominant along the contact between the upper and lower amphibolite groups in the vicinity of the magnetic marker (Fig. 2).

3. Petrography

Mafic amphibolites are composed of hornblende (60–80%) + plagioclase (5–20%) + quartz (5–20%) + titanite (0–2%) ± Fe–Ti oxides (0–5%) ± apatite (<1%) (Fig. 4(a)).

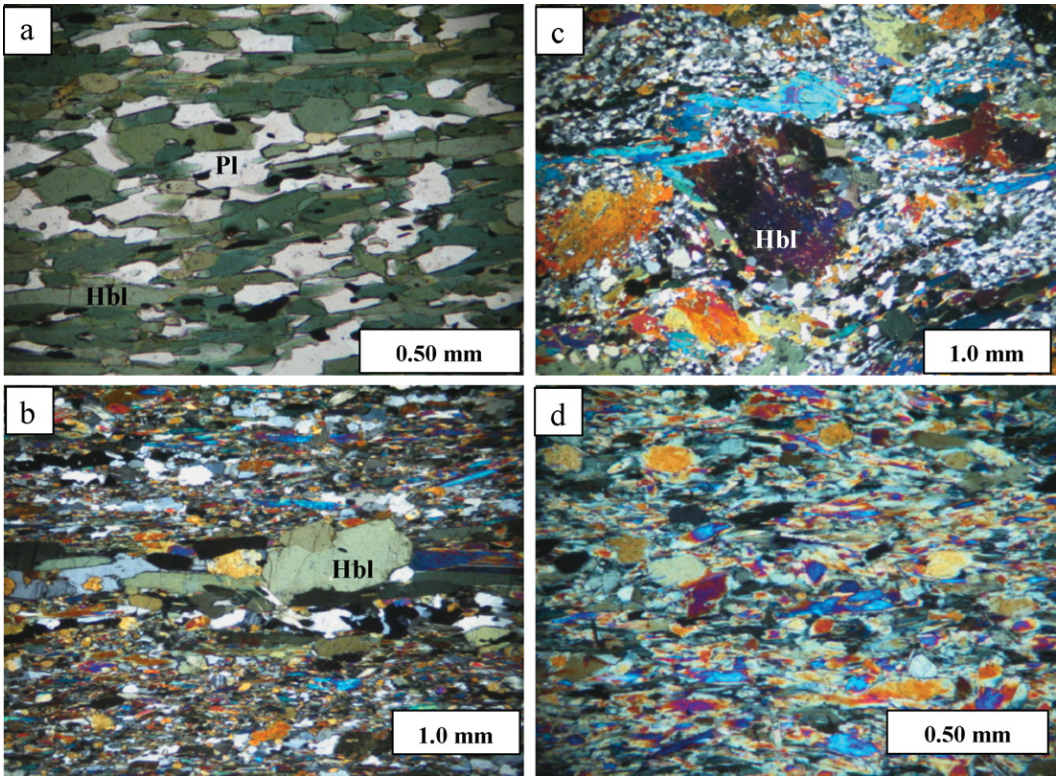

Fig. 4. Photomicrographs of metavolcanic rocks. (a) Mafic amphibolites with characteristic foliation defined by oriented hornblende. (b) Mylonitic amphibolite with recrystallized ribbons of hornblende. (c) Mylonitic amphibolite with deformed porphyroclasts of hornblende embedded in a dynamically recrystallized groundmass. (d) Actinolite-rich ultramafic amphibolite. Plane polarized light for (a). Crossed polarized light for (b–d). Abbreviations: Hbl, hornblende; Pl, plagioclase.

Biotite and fibrolitic actinolite and tremolite locally replace hornblende. In some locations amphibole is replaced by epidote and diopside. These calc-silicate minerals occur as disseminations and as thin layers (1–5 mm) concordant to the prevalent foliation. Amphibolites with mylonitic fabrics are locally present. They contain hornblende porphyroclasts with undulose extinction, subgrains, and kink folding (Fig. 4 (b and c)).

Ultramafic amphibolites are composed primarily of actinolite, with minor tremolite and hornblende (<10%) (Fig. 4(d)). Actinolite and tremolite form aggregates with preferential orientation. Some ultramafic amphibolites are partially to completely replaced by chlorite. Calcite and biotite are occasionally associated with this alteration. Mylonitic fabrics similar to those displayed by the mafic amphibolites are also present in ultramafic amphibolites.

Detailed petrographic description of stage-I calc-silicates are given in Polat et al. (2007a). The stage-II calc-silicate rocks are of stratabound appearance, replacing the mafic and ultramafic amphibolites, and gabbroic dykes (Fig. 3(c–f)). They are composed of diopside (10–80%) + epidote (30–85%) + quartz (1–20%) + plagioclase (0–5%) ± garnet (0–5%) ± Fe–Ti oxides (<1%) ± titanite (<1%) ± calcite (<1%) (Table 1, Fig. 5(a–f)). Scheelite and vesuvianite have been documented by Appel (1983, 1994, 1997).

The stage-II calc-silicates include two phases of prograde (assemblages IIa, IIb) and one phase of retrograde (assemblage IIc) metamorphism (Table 1). The prograde

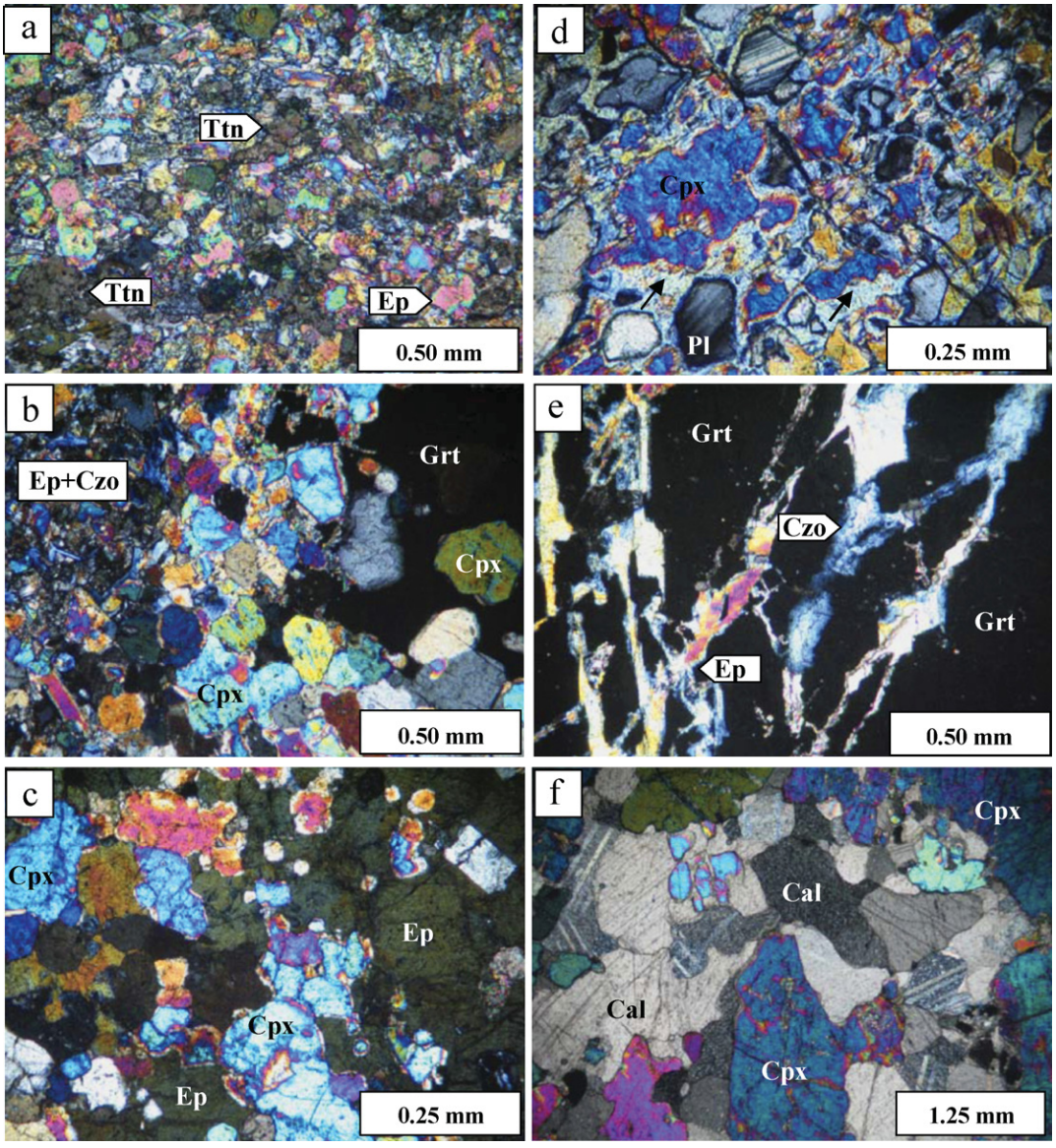

Fig. 5. Photomicrographs of stage-II calc-silicate assemblages (crossed polarized light). (a) Fine-grained epidote-rich metasomatic assemblage IIa. (b) Coarse-grained garnet-clinopyroxene assemblage IIb overprinting the fine-grained assemblage IIa. (c) Patchy epidote (metasomatic assemblage IIc) replacing clinopyroxene of the assemblage IIb. (d) Relict clinopyroxene and plagioclase partially replaced by epidote (arrows) of the assemblage IIc. (e) Fine veinlets of epidote and clinozoisite replacing fractured garnet porphyroblast. (f) Calcite overprinting the assemblage IIb. Abbreviations: Ttn, titanite; Ep, epidote; Grt, garnet; Cpx, clinopyroxene; Czo, clinozoisite; Cal, calcite.

metasomatic assemblage IIa is characterized by fine-grained aggregates of epidote + clinozoisite + clinopyroxene + quartz + plagioclase + titanite ± apatite (Fig. 5(a)). Clinopyroxene is rich in diopside component (Polat et al., 2007a). This assemblage is the most abundant and occurs as concordant (relative to the regional foliation) boudinaged layers replacing the mafic and ultramafic amphibolites.

The prograde metasomatic assemblage IIb consists of coarse-grained clinopyroxene (second generation) and garnet (Fig. 5(b)). Garnet is composed of grossular-andradite, and clinopyroxene is dominated by diopside (Polat et al., 2007a). The assemblage IIb replaces the epidote-rich metasomatic assemblage IIa. Diopside and garnet have smooth contacts indicating growth at equilibrium conditions. Diopside also forms massive pods of coarse-grained (up to 4 cm) crystals overprinting the metasomatic assemblage IIa.

The retrograde metasomatic assemblage IIc consists predominantly of epidote (second generation) with minor quartz, amphibole, and calcite. This assemblage occurs as patchy alterations and brittle veins (Table 1). Coarse-grained patchy epidote overprints earlier assemblages (IIa and IIb) and contains relict skeletal inclusions of garnet, diopside, and idioblastic titanite (Fig. 5(c)). This assemblage shows cataclastic texture with angular porphyroclasts of diopside, quartz, and plagioclase (assemblages IIa and IIb) cemented by a groundmass of late epidote, clinozoisite, and minor calcite (Fig. 5(d)). Tremolite is locally associated with this assemblage and mantles diopside. Epidote veins are highly discordant and crosscut amphibolites, stage-I calc-silicates, and calc-silicate assemblages IIa and IIb. Fine veinlets (<0.5 mm) of epidote and rare calcite crosscut the prograde assemblages (Fig. 5(e and f)).

4. Analytical methods and data presentation

Samples were pulverized using an agate mill in the Department of Earth and Environmental Sciences of the University of Windsor, Canada. Major elements and some trace elements (Sc and Zr) were analyzed on a Thermo Jarrel-Ash ENVIRO II ICP-OES by Activation laboratories Ltd. (ATCLABS) in Ancaster, Canada. The samples were mixed with a flux of lithium metaborate and lithium tetraborate, and fused at 1000 °C in an induction furnace. The molten beads were rapidly digested in a solution of 5% HNO_3 containing an internal standard, and mixed continuously until complete dissolution. Totals of major elements are 100 ± 1 wt.% and their analytical precisions are of 1–2%. The analytical precisions for Sc and Zr are better than 5%.

Transition metals (Ni, Co, Cr, and V), REE, HFSE, and LILE were analyzed on a high-sensitivity Thermo Elemental X7 ICP-MS in the Great Lakes Institute for Environmental Research (GLIER), University of Windsor, Canada, following the protocols of Jenner et al. (1990). Samples dissolution was conducted under clean lab conditions with double distilled acids. Approximately 100–130 mg of sample powder was used for acid digestion. Samples were dissolved in Teflon bombs in a concentrated mixture of HF–HNO_3 at a temperature of 120 °C for 3 days and then further attacked with 50% HNO_3 until no visible solid residue was left. Hawaiian basalt standards BHVO-1 and BHVO-2 were used as reference materials to estimate precision and accuracy. Analytical precisions are estimated as follows: 3–10% for REE, Y, Nb, Rb, Sr, Cs, Ba, Cu, and Co; 10–20% for Li, Ni, Zn, Ta, Th, and U; and 20–30% for Pb, V, and Cr.

Major element analyses were recalculated to 100 wt.% anhydrous basis for inter-comparisons. Chondrite and primitive mantle reservoir compositions are those of Sun and McDonough (1989) and Hofmann (1988), respectively. The Eu (Eu/Eu^*), Ce (Ce/Ce^*), Nb (Nb/Nb^*), and Zr (Zr/Zr^*) anomalies were calculated with respect to the neighboring immobile elements, following the method of Taylor and McLennan (1985). These geochemical anomalies are used for petrogenesis only in samples with near-primary magmatic composition. Mg-numbers (%) were calculated as the molecular ratio of $Mg^{2+}/(Mg^{2+} + Fe^{2+})$ where Fe^{2+} is assumed to be 90% of the total Fe.

5. Geochemical results

5.1. Mafic amphibolites

Mafic amphibolites are characterized by Mg-numbers ranging from 43 to 67. They have variable SiO_2 (42.9–56.9 wt.%), MgO (4.6–11.4 wt.%), Na_2O (0.80–4.0 wt.%), K_2O (<0.01–0.87 wt.%), Fe_2O_3 (7.1–20.6 wt.%), and CaO (7.3–14.7 wt.%) contents. Zirconium ranges from 31 to 95 ppm (Figs. 6 and 7; Table 2). They do not display significant correlations on Zr versus Na_2O, K_2O, Fe_2O_3, and LILE (Rb, Sr, and Pb) diagrams (Figs. 6 and 7). Niobium, Th, and LREE show variably scattered patterns on Zr variation diagrams. In contrast, HREE, Al_2O_3, TiO_2, Ni, Sc, V, and Co show good correlation with Zr. The majority of samples possess Zr/Y ratios similar to those found in modern tholeiitic basalts (1.0–3.7 vs. <2.0–4.5 in tholeiites) (cf. Barrett and MacLean, 1994).

Mafic amphibolites can be subdivided into four groups on the basis of the trace element systematics (Fig. 8). Group 1 amphibolites display near-flat REE patterns ($La/Yb_{cn} = 0.8–1.1$). They possess negative Nb ($Nb/Nb^* = 0.42–0.67$), and negative to slightly positive Ti ($Ti/Ti^* = 0.67–1.14$) and Zr ($Zr/Zr^* = 0.83–1.19$) anomalies (Table 2; Fig. 8(a and b)). The europium anomalies ($Eu/Eu^* = 0.88–1.05$) are not pronounced.

Group 2 amphibolites are characterized by U-shape REE patterns ($La/Sm_{cn} = 2.6–3.0$, $Gd/Yb_{cn} = 0.28–0.43$). They display positive Nb ($Nb/Nb^* = 1.3–1.5$) and Eu ($Eu/Eu^* = 1.95–2.32$) anomalies, and strong negative to positive Ti ($Ti/Ti^* = 0.23–6.27$) and Zr ($Zr/Zr^* = 0.41–8.2$) anomalies (Table 2; Fig. 8(c and d)).

Group 3 amphibolites display variably depleted LREE patterns ($La/Sm_{cn} = 0.3–0.9$). They possess negative Nb ($Nb/Nb^* = 0.2–0.9$), and negative to positive Ti ($Ti/Ti^* = 0.35–1.17$), Zr ($Zr/Zr^* = 0.79–1.17$), and Eu ($Eu/Eu^* = 0.55–1.10$) anomalies (Fig. 8(e and f)).

Group 4 amphibolites have positively fractionated REE patterns ($La/Yb_{cn} = 1.0–3.5$; $Gd/Yb_{cn} = 1.5–1.6$). They exhibit negative to positive Zr ($Zr/Zr^* = 0.58–1.18$) anomalies, and negative Nb ($Nb/Nb^* = 0.22–0.54$), Ti ($Ti/Ti^* = 0.72–0.88$), and Eu ($Eu/Eu^* = 0.89–0.91$) anomalies.

Table 2
Major (wt.%) and trace element (ppm) concentrations and significant element ratios for mafic and ultramafic amphibolites and calc-silicate rocks

	Group-1 amphibolites									Group-2 amphibolites		
	485405	485409	496114	485414	485416	485425	496119	496120	496121	485402	485403	485406
SiO_2	51.25	50.62	49.38	50.65	52.45	56.86	48.22	50.84	55.30	50.74	52.74	49.75
TiO_2	1.04	1.59	1.74	0.75	0.81	0.52	0.78	0.79	0.70	1.34	1.42	0.07
Al_2O_3	14.60	13.98	11.06	15.23	15.85	15.22	15.87	15.47	13.90	14.61	13.49	13.43
Fe_2O_3	12.03	14.85	19.00	11.58	9.41	7.08	12.73	9.75	9.46	11.46	10.21	14.11
MnO	0.19	0.22	0.30	0.18	0.22	0.17	0.20	0.20	0.18	0.13	0.13	0.17
MgO	8.14	5.67	5.67	7.62	4.59	6.46	8.27	7.57	7.73	10.15	10.26	11.40
CaO	10.12	9.53	9.23	12.46	14.71	12.45	11.91	13.90	11.19	7.41	7.96	6.11
Na_2O	2.36	2.95	2.80	1.39	1.71	1.08	1.74	1.25	1.36	3.70	3.45	3.18
K_2O	0.08	0.33	0.57	0.08	0.18	0.11	0.21	0.17	0.13	0.46	0.35	LDL
P_2O_5	0.19	0.26	0.26	0.05	0.07	0.04	0.06	0.06	0.06	LDL	LDL	1.78
LOI	0.79	0.36	0.50	0.85	0.69	0.52	0.67	0.69	0.68	1.98	1.61	0.09
Mg-number	57	43	37	57	49	64	56	61	62	64	67	62
Sc	35	43	47	43	42	44	44	41	36	47	46	77
V	195	256	299	243	272	217	278	245	221	308	266	LDL
Cr	245	104	190	122	981	2030	275	269	235	129	116	197
Co	42	39	34	49	53	51	53	53	48	37	35	46
Ni	92	70	105	117	187	218	236	274	232	73	72	75
Rb	1.0	6.4	24.0	1.1	2.4	1.6	1.5	0.5	1.1	52.5	48.6	3.2
Sr	129.7	119.6	21.6	126.1	115.1	46.9	84.4	118.0	116.7	52.9	53.6	34.2
Y	25.5	32.7	28.5	15.3	18.0	14.5	15.6	16.5	14.8	6.3	6.9	7.8
Zr	94.8	76.4	59.1	42.4	42.4	31.5	40.5	42.6	37.1	71.5	80.1	7.1
Nb	2.45	2.48	2.21	1.61	1.76	1.36	1.37	1.49	1.29	1.00	0.96	2.21
Cs	0.05	0.38	3.33	0.14	0.27	0.29	0.06	LDL	0.21	7.26	6.71	3.22
Ba	17.4	47.4	53.4	17.5	24.3	31.4	14.2	25.0	23.1	60.2	56.1	13.7
Ta	0.15	0.17	0.14	0.11	0.12	0.08	0.10	0.11	0.10	0.10	0.10	0.19
Pb	2.01	6.59	4.50	1.88	1.57	2.79	3.63	2.18	1.35	1.76	1.71	1.51
Th	0.60	0.68	0.61	0.37	0.40	0.66	0.47	0.36	0.32	0.05	0.04	0.20
U	0.13	0.17	0.11	0.06	0.16	0.16	0.06	0.07	0.06	0.02	0.02	0.03
La	4.09	5.86	4.57	2.57	2.82	2.63	2.06	2.75	2.28	1.49	1.74	2.41
Ce	12.03	15.56	11.83	6.98	7.64	6.43	6.05	7.61	6.21	2.62	3.34	5.03
Pr	1.90	2.30	1.82	1.11	1.18	0.89	0.90	1.12	0.95	0.29	0.39	0.58
Nd	9.82	11.47	9.14	5.54	6.17	4.54	4.71	5.81	5.01	1.19	1.62	2.45
Sm	3.14	3.57	3.03	1.90	2.08	1.36	1.69	1.88	1.64	0.31	0.42	0.59
Eu	1.24	1.35	1.10	0.70	0.74	0.50	0.57	0.66	0.58	0.29	0.33	0.45
Gd	4.18	5.06	4.25	2.45	2.76	2.12	2.28	2.57	2.23	0.46	0.61	0.80
Tb	0.71	0.88	0.75	0.43	0.47	0.37	0.41	0.45	0.40	0.10	0.10	0.14
Dy	4.70	5.85	5.06	2.93	3.20	2.66	2.83	3.03	2.72	0.78	0.93	1.08
Ho	1.01	1.30	1.09	0.60	0.70	0.58	0.61	0.64	0.59	0.22	0.24	0.28
Er	2.99	3.85	3.32	1.85	2.16	1.73	1.82	1.94	1.73	0.85	0.90	1.04
Tm	0.43	0.54	0.48	0.26	0.33	0.26	0.26	0.28	0.25	0.16	0.17	0.18
Yb	2.83	3.56	3.28	1.70	2.08	1.68	1.72	1.86	1.61	1.36	1.50	1.51
Lu	0.43	0.54	0.51	0.25	0.31	0.27	0.26	0.27	0.24	0.26	0.27	0.27
$(La/Yb)_{cn}$	0.97	1.11	0.94	1.02	0.91	1.05	0.81	1.00	0.95	0.74	0.78	1.07
$(La/Sm)_{cn}$	0.82	1.03	0.95	0.85	0.85	1.22	0.77	0.92	0.87	2.99	2.58	2.55
$(Gd/Yb)_{cn}$	1.20	1.15	1.05	1.17	1.07	1.02	1.07	1.12	1.12	0.28	0.33	0.43

$(Eu/Eu^*)_{cn}$	1.05	0.97	0.94	0.99	0.94	0.90	0.88	0.92	0.93	2.32	1.95	2.01
$(Ce/Ce^*)_{cn}$	1.04	1.02	0.99	0.99	1.01	1.01	1.07	1.04	1.02	0.96	0.97	1.02
Al_2O_3/TiO_2	14.05	8.78	6.36	20.31	19.60	29.11	20.47	19.59	19.93	10.92	9.47	191.01
Nb/Ta	15.97	14.84	15.65	14.47	14.43	17.09	13.78	13.61	12.75	10.03	9.58	11.61
Zr/Y	3.71	2.34	2.08	2.77	2.35	2.17	2.60	2.58	2.51	11.43	11.67	0.92
Ti/Zr	65.69	124.95	176.29	106.05	114.33	99.40	114.80	111.13	112.74	112.11	106.60	59.09
Nb/Nb^*	0.64	0.51	0.54	0.67	0.67	0.42	0.57	0.61	0.62	1.51	1.52	1.29
Zr/Zr^*	1.19	0.83	0.79	0.91	0.83	0.89	1.00	0.90	0.91	8.20	6.76	0.41
Ti/Ti^*	0.73	0.90	1.14	0.85	0.84	0.67	0.92	0.87	0.86	6.27	5.87	0.23
$\sum$REE	49.50	61.70	50.23	29.29	32.64	26.02	26.17	30.87	26.44	10.39	12.57	16.82
North	64°43.838′	64°43.631′	64°43.657′	64°44.055′	64°44.069′	64°44.920′	64°43.927′	64°44.058′	64°44.005′	64°43.803′	64°43.803′	64°43.877′
West	49°55.618′	49°55.799′	49°56.762′	49°56.286′	49°56.307′	49°57.202′	49°56.222′	49°56.756′	49°57.191′	49°55.723′	49°55.723′	49°55.729′

	Group-3 amphibolites									Goup-4 amphibolites	
	485401	485407	496116	496117	496118	496123	485404	485415	496122	485410	496115
SiO_2	42.88	48.09	48.09	48.57	48.33	52.18	50.04	52.31	48.70	52.90	55.14
TiO_2	1.14	0.61	0.93	0.65	0.61	0.98	1.61	1.09	0.50	0.91	0.86
Al_2O_3	12.74	13.45	16.82	15.42	15.25	14.23	13.87	18.27	16.56	13.73	14.83
Fe_2O_3	20.55	14.53	13.50	13.59	12.84	13.58	15.62	10.06	10.71	10.61	10.63
MnO	0.15	0.13	0.14	0.19	0.21	0.21	0.23	0.20	0.21	0.23	0.13
MgO	8.76	6.77	6.79	8.84	8.47	6.46	6.62	4.37	9.93	6.23	6.79
CaO	12.89	14.50	9.44	10.40	13.13	11.21	9.41	9.60	10.96	11.40	7.25
Na_2O	0.90	1.77	3.34	2.13	1.08	0.80	2.15	3.89	2.07	3.33	4.00
K_2O	LDL	0.13	0.87	0.15	0.05	0.26	0.26	0.17	0.32	0.50	0.24
P_2O_5	LDL	0.02	0.08	0.05	0.04	0.08	0.19	0.05	0.04	0.17	0.12
LOI	0.73	0.80	0.77	0.99	0.95	0.48	0.62	0.45	1.23	0.65	1.06
Mg-number	46	48	50	56	57	48	46	46	65	54	56
Sc	35	24	40	46	50	48	42	50	42	47	31
V	399	312	273	262	278	327	327	321	216	304	214
Cr	73	151	119	252	395	138	133	233	301	405	255
Co	58	49	48	56	58	48	43	67	54	43	41
Ni	97	101	106	227	239	139	74	180	279	123	128
Rb	2.8	2.9	42.3	1.4	3.4	1.3	8.4	2.6	62.6	3.7	6.4
Sr	119.4	127.7	92.1	88.5	53.8	104.5	93.4	74.4	123.6	154.4	129.0
Y	34.9	31.2	30.2	19.5	19.3	26.4	28.0	16.0	10.5	21.1	15.9
Zr	42.3	68.7	49.9	32.6	31.2	52.3	90.8	56.1	21.2	62.0	82.7
Nb	0.14	1.08	1.70	0.61	0.50	1.15	3.68	2.31	1.01	2.66	2.74
Cs	0.93	0.67	10.16	0.36	1.25	0.05	2.35	0.12	13.65	0.08	1.42
Ba	3.2	19.7	264.4	17.6	8.9	33.5	112.5	42.7	51.0	190.8	92.3
Ta	0.03	0.10	0.08	0.06	0.03	0.09	0.23	0.16	0.07	0.17	0.15
Pb	1.46	4.33	3.86	3.69	2.87	5.62	3.70	2.14	10.45	12.62	3.60
Th	0.06	0.44	0.45	0.18	0.12	0.31	0.81	0.42	0.15	1.98	1.75
U	0.04	0.21	0.11	0.10	0.04	0.09	0.19	0.11	0.04	0.50	0.30
La	1.16	2.25	1.78	1.33	1.04	2.46	3.93	2.81	1.38	11.79	2.42
Ce	4.21	6.87	4.83	3.87	3.00	6.53	11.79	7.65	3.92	24.67	11.47
Pr	0.84	1.30	0.85	0.59	0.51	1.05	1.92	1.19	0.58	3.34	1.61
Nd	5.54	8.03	5.01	3.36	3.04	5.61	9.94	5.81	3.09	14.85	8.59
Sm	2.56	3.39	2.22	1.41	1.34	2.14	3.27	1.95	1.12	3.73	2.79
Eu	0.62	0.76	0.64	0.53	0.50	0.72	1.18	0.82	0.40	1.16	0.87

Table 2 (*Continued*)

	Group-1 amphibolites									Group-2 amphibolites		
	485405	485409	496114	485414	485416	485425	496119	496120	496121	485402	485403	485406
Gd	4.55	4.85	3.78	2.31	2.25	3.54	4.55	2.65	1.56	4.13	3.19	
Tb	0.86	0.86	0.73	0.46	0.45	0.66	0.76	0.46	0.29	0.64	0.50	
Dy	6.14	5.82	5.24	3.24	3.23	4.59	5.14	3.11	1.91	4.08	3.14	
Ho	1.36	1.26	1.18	0.75	0.74	1.01	1.09	0.67	0.42	0.82	0.63	
Er	4.10	3.66	3.67	2.32	2.34	3.15	3.22	2.01	1.24	2.42	1.79	
Tm	0.58	0.50	0.55	0.35	0.34	0.46	0.47	0.30	0.18	0.34	0.24	
Yb	3.83	3.14	3.62	2.36	2.32	3.06	3.10	1.86	1.17	2.26	1.58	
Lu	0.56	0.45	0.54	0.36	0.34	0.46	0.46	0.28	0.18	0.32	0.24	
$(La/Yb)_{cn}$	0.20	0.48	0.33	0.38	0.30	0.54	0.85	1.02	0.79	3.51	1.03	
$(La/Sm)_{cn}$	0.28	0.42	0.50	0.59	0.49	0.72	0.76	0.91	0.78	1.99	0.55	
$(Gd/Yb)_{cn}$	0.96	1.25	0.84	0.79	0.78	0.93	1.18	1.15	1.08	1.48	1.63	
$(Eu/Eu^*)_{cn}$	0.55	0.57	0.68	0.90	0.88	0.79	0.93	1.10	0.92	0.91	0.89	
$(Ce/Ce^*)_{cn}$	1.03	0.97	0.94	1.05	0.99	0.98	1.03	1.01	1.05	0.95	1.40	
Al_2O_3/TiO_2	11.22	22.22	18.06	23.58	25.06	14.56	8.64	16.77	32.99	15.17	17.22	
Nb/Ta	4.60	10.37	22.50	10.80	14.28	12.34	15.92	14.88	14.14	15.56	17.81	
Zr/Y	1.21	2.20	1.65	1.67	1.62	1.98	3.25	3.51	2.01	2.94	5.21	
Ti/Zr	161.01	52.81	111.87	120.46	117.00	112.06	106.04	116.41	142.17	87.51	62.47	
Nb/Nb^*	0.22	0.45	0.78	0.50	0.57	0.54	0.84	0.86	0.90	0.22	0.54	
Zr/Zr^*	0.79	0.92	1.05	1.05	1.08	1.06	1.11	1.17	0.80	0.58	1.18	
Ti/Ti^*	0.63	0.35	0.61	0.69	0.65	0.72	1.04	1.17	0.86	0.72	0.88	
$\sum$REE	36.93	43.15	34.64	23.24	21.44	35.45	50.83	31.56	17.43	74.57	39.04	
North	64°43.771′	64°43.877′	64°43.839′	64°43.849′	64°43.904′	64°43.953′	64°43.813′	64°44.062′	64°43.891′	64°43.623′	64°43.764′	
West	49°55.605′	49°55.729′	49°56.668′	49°56.814′	49°56.527′	49°56.600′	49°55.612′	49°56.298′	49°57.609′	49°55.941′	49°56.692′	

	Ultramafic amphibolites		Calc-silicate rocks							
	499742	499743	496110*	496111*	496113*	499717*	496112	485411	499718	485439
SiO_2	49.35	49.19	55.14	54.37	56.98	47.42	46.54	54.37	46.51	50.62
TiO_2	0.36	0.36	0.90	0.87	0.89	0.64	0.69	0.87	0.17	0.24
Al_2O_3	8.38	8.30	16.16	16.36	16.35	15.67	12.55	16.36	2.46	5.86
Fe_2O_3	11.51	11.59	8.21	7.65	5.71	11.43	8.30	7.65	9.02	7.90
MnO	0.20	0.20	0.15	0.13	0.11	0.23	0.35	0.13	0.64	0.30
MgO	19.07	18.91	2.40	2.37	2.03	2.87	6.32	2.37	10.57	9.77
CaO	9.43	9.78	16.20	17.23	14.99	21.51	24.76	17.23	30.42	25.00
Na_2O	1.39	1.44	0.73	0.91	2.73	0.11	0.29	0.91	0.16	0.18
K_2O	0.28	0.19	0.02	0.03	0.14	LDL	0.12	0.03	0.02	0.07
P_2O_5	0.03	0.03	0.08	0.08	0.07	0.11	0.06	0.08	0.03	0.05
LOI	2.04	1.91	1.42	2.52	2.32	1.38	1.15	2.52	6.21	1.96
Mg-number	77	76	37	38	41	33	60	38	70	71
Sc	27	28	37	41	45	29	36	23	6	23
V	147	149	317	279	305	305	215	77	41	123
Cr	1862	1896	250	375	208	245	168	73	47	6415
Co	77	77	29	43	46	40	45	16	11	90
Ni	819	820	141	198	209	239	189	71	29	976
Rb	20.9	6.0	1.1	0.2	0.7	0.2	12.0	6.3	0.2	7.5
Sr	112.0	112.6	320.1	204.4	197.0	321.3	112.2	113.6	55.6	1773.8

Y	10.7	9.7	19.4	17.9	13.4	30.2	15.1	19.3	4.7	4.9
Zr	24.3	27.7	60.1	55.1	46.9	37.6	39.4	43.4	8.6	11.4
Nb	0.99	0.94	2.05	2.11	1.64	1.54	1.41	0.17	0.54	0.62
Cs	10.41	3.10	0.10	0.08	0.06	0.06	5.50	11.63	0.37	0.46
Ba	61.2	19.4	11.5	8.1	27.0	12.5	16.4	18.0	3.5	67.4
Ta	0.09	0.09	0.15	0.16	0.12	0.11	0.11	0.04	0.04	0.04
Pb	3.61	3.21	10.12	4.96	3.30	15.62	2.30	3.71	2.55	22.27
Th	0.75	0.87	0.67	0.70	0.34	0.36	0.31	0.21	0.13	0.17
U	0.22	0.23	0.16	0.16	0.19	0.18	0.16	0.02	0.13	0.05
La	3.24	3.30	4.72	4.58	2.80	5.82	2.73	0.65	0.89	1.51
Ce	7.78	8.26	11.44	11.77	7.45	14.06	7.17	3.00	1.64	2.77
Pr	1.01	0.94	1.65	1.66	1.13	2.09	1.10	0.71	0.21	0.38
Nd	4.39	3.98	7.82	7.97	5.61	10.64	5.53	4.44	1.04	1.82
Sm	1.15	1.08	2.42	2.35	1.83	3.49	1.75	1.91	0.33	0.53
Eu	0.30	0.31	1.25	0.80	0.67	1.24	0.56	0.30	0.18	0.32
Gd	1.43	1.37	3.09	3.03	2.28	4.79	2.16	2.76	0.46	0.74
Tb	0.27	0.24	0.54	0.52	0.40	0.78	0.39	0.51	0.08	0.13
Dy	1.78	1.66	3.56	3.48	2.60	4.94	2.59	3.49	0.59	0.92
Ho	0.38	0.36	0.75	0.71	0.53	1.01	0.56	0.76	0.15	0.21
Er	1.24	1.10	2.23	2.12	1.54	2.84	1.74	2.33	0.49	0.61
Tm	0.18	0.16	0.32	0.30	0.22	0.38	0.24	0.34	0.07	0.09
Yb	1.28	1.10	2.12	1.95	1.39	2.29	1.67	2.22	0.46	0.57
Lu	0.21	0.17	0.31	0.29	0.20	0.32	0.25	0.34	0.08	0.09
$(La/Yb)_{cn}$	1.70	2.02	1.50	1.58	1.36	1.71	1.10	0.20	1.30	1.78
$(La/Sm)_{cn}$	1.76	1.93	1.23	1.22	0.96	1.05	0.98	0.21	1.70	1.78
$(Gd/Yb)_{cn}$	0.90	1.00	1.18	1.26	1.33	1.69	1.05	1.01	0.80	1.05
$(Eu/Eu^*)_{cn}$	0.71	0.77	1.40	0.91	1.01	0.93	0.88	0.40	1.43	1.56
$(Ce/Ce^*)_{cn}$	1.04	1.13	0.99	1.03	1.01	0.97	1.00	1.07	0.91	0.88
Al_2O_3/TiO_2	23.19	22.82	17.92	18.75	18.30	24.55	18.15	18.75	14.71	24.13
Nb/Ta	11.49	10.72	13.46	13.16	13.54	13.88	12.34	4.89	12.30	15.09
Zr/Y	2.28	2.86	3.09	3.08	3.49	1.25	2.62	2.25	1.84	2.33
Ti/Zr	89.18	78.82	89.92	94.92	114.30	101.91	105.30	120.53	116.15	128.07
Nb/Nb^*	0.26	0.23	0.47	0.48	0.69	0.43	0.62	0.19	0.65	0.51
Zr/Zr^*	0.75	0.94	0.97	0.89	1.02	0.43	0.89	1.04	1.03	0.81
Ti/Ti^*	0.67	0.73	0.83	0.83	1.12	0.42	0.88	0.84	0.96	0.90
$\sum$REE	24.64	24.02	42.21	41.52	28.68	54.70	28.43	23.76	6.68	10.70
North	64°44.878′	64°44.878′	64°44.453′	64°44.460′	64°44.338′	64°44.458′	64°44.402′	64°43.691′	64°44.564′	64°44.859′
West	49°53.758′	49°53.758′	49°52.106′	49°52.433′	49°54.278′	49°52.393′	49°53.298′	49°55.570′	49°51.967′	49°53.752′

	Calc-silicate rocks							Average chemically zoned pillows[a]		
	485440	499715	499716	499740	499741	496105	485471	Pillow rims	Outer pillows	Inner pillows
SiO_2	48.66	43.42	49.78	45.60	48.72	49.11	54.53	48.50	55.70	52.10
TiO_2	0.31	1.84	1.80	0.31	0.72	0.33	0.43	0.55	0.54	0.53
Al_2O_3	7.68	15.98	1.03	12.17	7.25	6.15	10.64	14.19	14.47	14.08
Fe_2O_3	8.94	10.88	14.94	11.18	8.59	13.02	8.87	12.31	8.41	8.34
MnO	0.34	0.16	0.33	0.27	0.34	0.38	0.26	0.23	0.18	0.21
MgO	8.89	3.30	8.48	6.70	9.49	8.66	5.79	9.51	6.45	4.59
CaO	24.59	24.23	23.25	23.51	23.51	22.07	18.83	12.79	12.40	19.59
Na_2O	0.52	0.09	0.33	0.16	0.25	0.15	0.46	1.66	1.68	0.51
K_2O	0.06	LDL	0.06	0.06	0.11	0.09	0.15	0.17	0.13	0.01

Table 2 (*Continued*)

	Calc-silicate rocks							Average chemically zoned pillows[a]		
	485440	499715	499716	499740	499741	496105	485471	Pillow rims	Outer pillows	Inner pillows
P_2O_5	0.03	0.11	0.01	0.03	0.01	0.04	0.04	0.04	0.04	0.04
LOI	1.67	1.09	0.01	1.42	0.80	0.36	0.66	0.92	1.17	0.91
Mg-number	66	38	53	54	69	57	56	60	60	52
Sc	23	36	62	26	52	22	29	44.5	43.8	43.5
V	151	332	129	203	139	138	174	224	227	213
Cr	8290	1035	168	1780	1863	88	229	328.97	307.09	721.71
Co	106	66	81	100	152	55	46	74.14	60.88	66.27
Ni	1152	714	416	1391	2292	138	110	249.12	233.49	325.18
Rb	9.7	0.6	14.3	0.6	0.8	0.7	14.5	3.77	2.33	2.22
Sr	1182.9	336.5	55.6	1991.8	1302.9	39.9	68.9	85.80	86.93	94.14
Y	6.8	50.3	26.1	7.6	3.4	8.5	13.1	14.01	13.19	12.25
Zr	16.3	90.6	113.4	25.8	30.6	27.9	18.1	33.2	31.4	30.3
Nb	1.43	42.54	22.39	3.21	12.36	1.37	1.31	1.12	1.20	1.16
Cs	8.84	0.34	0.38	0.28	0.30	0.33	1.05	0.47	0.12	0.53
Ba	60.2	11.7	285.5	12.9	62.9	5.5	53.9	49.72	43.07	21.89
Ta	0.06	7.01	1.79	0.05	0.14	0.07	0.04	0.09	0.08	0.08
Pb	19.12	12.47	5.52	35.85	31.35	3.77	4.13	4.36	4.49	6.57
Th	0.23	1.14	0.88	0.56	0.33	0.16	0.20	0.68	0.69	0.63
U	0.06	1.91	1.81	0.16	0.61	0.05	0.06	0.15	0.24	0.23
La	1.69	9.77	6.85	1.77	1.45	0.98	1.40	2.32	3.09	2.84
Ce	3.49	21.92	20.76	3.45	2.78	2.76	3.59	6.07	7.43	6.57
Pr	0.47	3.12	3.08	0.47	0.38	0.40	0.53	0.86	1.01	0.90
Nd	2.10	14.76	14.33	2.34	1.62	2.11	2.59	4.19	4.61	4.28
Sm	0.68	5.48	3.76	0.89	0.46	0.82	0.92	1.36	1.37	1.33
Eu	0.22	1.81	1.52	1.21	0.22	0.23	0.34	0.46	0.50	0.50
Gd	0.91	6.99	4.38	1.20	0.54	1.19	1.57	2.01	1.99	1.86
Tb	0.16	1.20	0.72	0.21	0.10	0.21	0.29	0.37	0.35	0.34
Dy	1.19	7.86	4.68	1.41	0.70	1.37	2.15	2.49	2.42	2.35
Ho	0.29	1.64	0.98	0.29	0.15	0.30	0.48	0.55	0.52	0.50
Er	0.94	5.05	2.96	0.85	0.47	0.91	1.43	1.62	1.57	1.49
Tm	0.14	0.77	0.44	0.12	0.07	0.13	0.21	0.24	0.23	0.22
Yb	0.94	5.21	3.21	0.79	0.50	0.86	1.47	1.59	1.53	1.46
Lu	0.16	0.75	0.52	0.12	0.08	0.13	0.22	0.24	0.23	0.22
$(La/Yb)_{cn}$	1.21	1.26	1.44	1.51	1.97	0.77	0.64	0.98	1.36	1.31
$(La/Sm)_{cn}$	1.55	1.12	1.15	1.25	1.97	0.75	0.95	1.07	1.41	1.34
$(Gd/Yb)_{cn}$	0.78	1.09	1.10	1.23	0.89	1.12	0.87	1.02	1.05	1.03
$(Eu/Eu^*)_{cn}$	0.84	0.89	1.14	3.58	1.32	0.70	0.86	0.85	0.93	0.98
$(Ce/Ce^*)_{cn}$	0.94	0.96	1.09	0.92	0.90	1.06	1.00	1.04	1.02	0.99
Al_2O_3/TiO_2	25.17	8.70	0.57	38.98	10.03	18.78	24.47	25.65	26.71	26.83
Nb/Ta	24.17	6.07	12.53	58.84	85.61	19.96	30.38	13.07	14.23	14.00
Zr/Y	2.38	1.80	4.35	3.39	9.00	3.27	1.38	2.37	2.38	2.47
Ti/Zr	112.41	121.63	95.40	72.66	141.61	70.44	143.88	99.82	103.36	103.82
Nb/Nb^*	0.94	5.19	3.72	1.31	7.28	1.40	1.01	0.36	0.33	0.35
Zr/Zr^*	0.95	0.70	1.08	1.25	2.47	1.48	0.82	0.97	0.87	0.89
Ti/Ti^*	0.89	0.77	1.26	0.73	3.45	0.79	0.70	0.74	0.75	0.76
$\sum$REE	13.38	86.33	68.19	15.10	9.52	12.40	17.19	24.37	26.84	24.86

North	64°44.859′	64°44.279′	64°44.339′	64°44.878′	64°44.878′	64°44.253′	64°44.814′	64°44.906′	64°44.906′	64°44.906′
West	49°53.752′	49°53.227′	49°52.738′	49°53.758′	49°53.758′	49°52.855′	49°51.504′	49°51.827′	49°51.827′	49°51.827′

LDL: Lower than detection limit.
[a] Averaged pillow basalt composition from Polat et al. (2007a).
[*] Calc-silicates with metasomatic assemblage IIa, other calc-silicate samples are variably overprinted by the assemblages IIb and IIc.

5.2. Ultramafic amphibolites

Ultramafic amphibolites are compositionally variable at 44.2–53.4 wt.% SiO_2, 15.5–25.6 wt.% MgO, 6.8–12.4 wt.% Fe_2O_3, 0.2–2.4 wt.% Na_2O, and 0.02–0.30 wt.% K_2O (Figs. 6 and 7). Mg-numbers range from 73 to 87. Low Zr contents (7–32 ppm) are consistent with an ultramafic composition. On Zr variation diagrams, TiO_2 and Al_2O_3 display positive correlations, whereas Ni shows a negative correlation (Figs. 6 and 7). They exhibit Zr/Y ratios mostly between 1.6 and 3.5 (Table 2).

Ultramafic amphibolites show variable characteristics on chondrite- and primitive mantle-normalized trace element diagrams (Fig. 9). Some ultramafic amphibolites have consistent negative Nb ($Nb/Nb^* = 0.23–0.40$) anomalies, slightly enriched LREE, and near-flat HREE ($La/Yb_{cn} = 1.7–3.3$; $Gd/Yb_{cn} = 0.8–1.2$) patterns (Fig. 9(a and b)). Other samples display negative to positive Nb ($Nb/Nb^* = 0.06–2.64$) anomalies, and depleted to highly enriched LREE ($La/Yb_{cn} = 0.44–22.1$) patterns (Fig. 9(c and d)).

5.3. Calc-silicate rocks

As a group, the stage-II calc-silicate rocks have highly variable geochemical characteristics (Figs. 6 and 7). Relative to the mafic and ultramafic amphibolites, they have comparable compositional ranges of SiO_2 (43–57 wt.%), TiO_2 (0.17–1.84 wt.%), Al_2O_3 (1.0–16.4 wt.%), Zr (9–113 ppm), and Y (3.4–50.3 ppm) (Table 3). They have higher CaO (15–30 wt.%), and lower MgO (2–11 wt.%), K_2O (<0.01–0.15 wt.%), and Fe_2O_3

Table 3
Selected compositional values and inter-element ratios for the least altered amphibolites and stage-II calc-silicate rocks

	Mafic amphibolites	Ultramafic amphibolites	Stage-II calc-silicates
Mg-number	37–64	73–83	33–71
SiO_2 (wt.%)	48–57	46–53	43–57
Fe_2O_3	7.1–19	9.0–11.6	5.7–14.9
MgO	4.6–8.3	15.5–21.8	2.0–10.6
CaO	9.2–14.7	9.4–11.4	15.0–30.4
Zr (ppm)	32–95	11–33	9–113
Ni	70–274	469–1211	29–2292
Sc	35–47	19–28	6–62
Cr	104–2030	1862–12,347	47–8290
ΣREE	26–62	12–25	7–86
$(La/Yb)_{cn}$	0.81–1.11	1.7–3.3	0.2–2.0
$(La/Sm)_{cn}$	0.77–1.22	1.6–3.4	0.2–2.0
$(Gd/Yb)_{cn}$	1.0–1.2	0.8–1.2	0.8–1.7
Al_2O_3/TiO_2	6.4–29.1	22.8–28.8	0.6–39
Nb/Ta	12.8–17.1	10.7–15.2	4.9–86
Zr/Y	2.1–3.7	2.3–3.2	1.3–9.0
Ti/Zr	65.7–176.3	79–108	70–144
$(Eu/Eu^*)_{cn}$	0.9–1.1	0.7–1.4	0.4–3.6
Nb/Nb^*	0.4–0.7	0.2–0.4	0.2–7.3
Zr/Zr^*	0.8–1.2	0.7–1.0	0.4–2.5
Ti/Ti^*	0.7–1.1	0.7–0.9	0.4–3.45

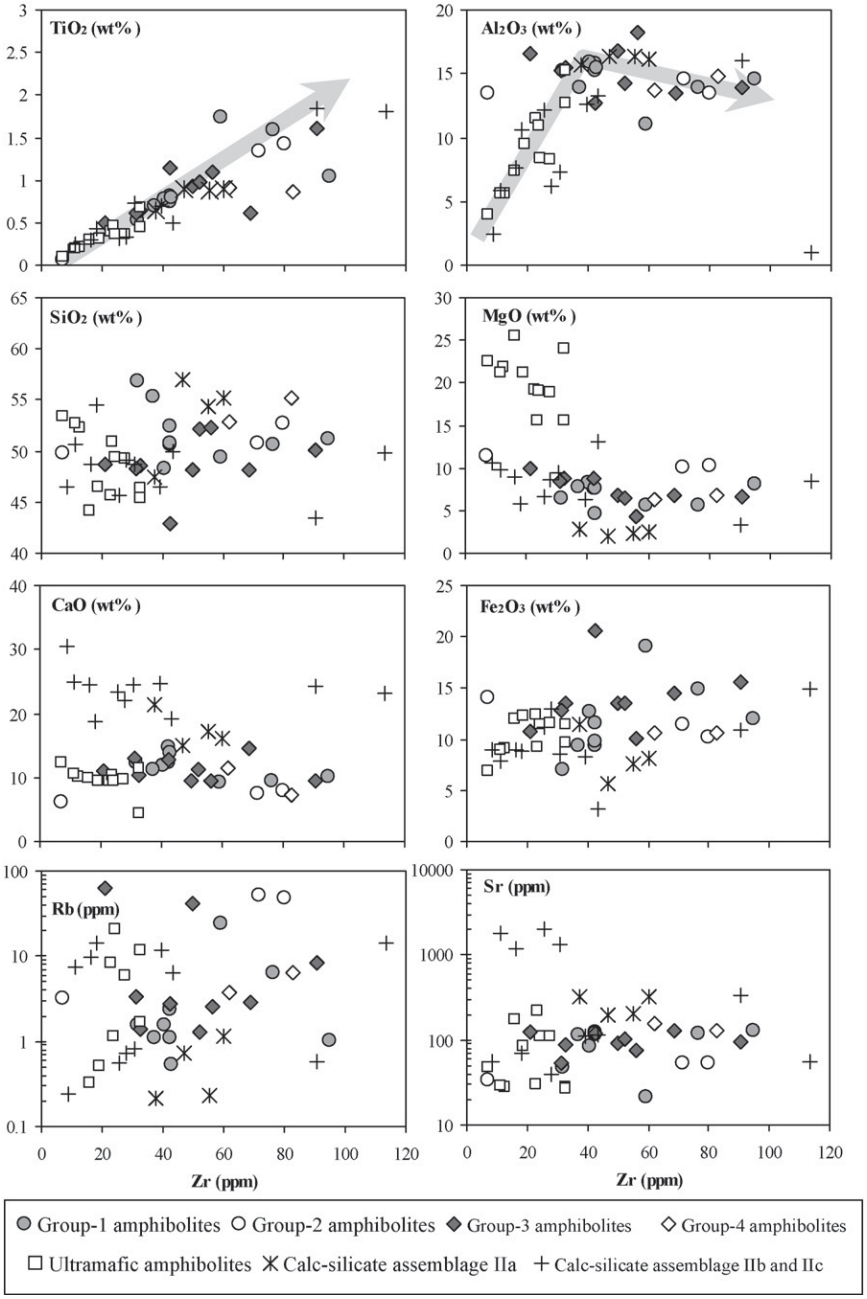

Fig. 6. Variation diagrams of Zr versus selected major elements and LILE. Ultramafic amphibolites from Polat et al. (2008) and this study (Table 2). Amphibolites and their associated calc-silicates have been plotted to show the chemical changes associated with the stage-II calc-silicate alteration. The amphibolites exhibit concentration levels of TiO_2, Al_2O_3, and MgO consistent with an ultramafic to mafic protolith. Arrows indicate differentiation trends (see text).

(5.7–14.9 wt.%) than amphibolites at a given Zr content. They have large variations in Na_2O (0.09–2.7 wt.%), MnO (0.10–0.64 wt.%), Sr (40–2000 ppm), and Pb (2–36 ppm) contents.

The calc-silicate rocks display variable trace element characteristics on chondrite- and primitive mantle-normalized diagrams (Fig. 10). They exhibit two distinct Nb anomalies: (1) negative ($Nb/Nb^* = 0.43–0.94$) (Fig. 10(b)), and (2) positive Nb ($Nb/Nb^* = 1.01–7.28$) anomalies (Fig. 10(d)). They have near-flat REE patterns with minor depletion or enrichment of LREE and HREE ($La/Yb_{cn} = 0.64–2.0$; $Gd/Yb_{cn} = 0.8–1.7$). They possess negative to positive Eu ($Eu/Eu^* = 0.7–3.6$), Ti ($Ti/Ti^* = 0.4–3.5$), and Zr ($Zr/Zr^* = 0.4–2.5$) anomalies. Sample 485411 displays a LREE-depleted trace element pattern similar to group 3 amphibolites (Fig. 10(c and d)).

6. Discussion

6.1. Regional metamorphism and metasomatism

The contrasting ages and complex metamorphic histories of the granite-greenstone associations of the Nuuk region have been

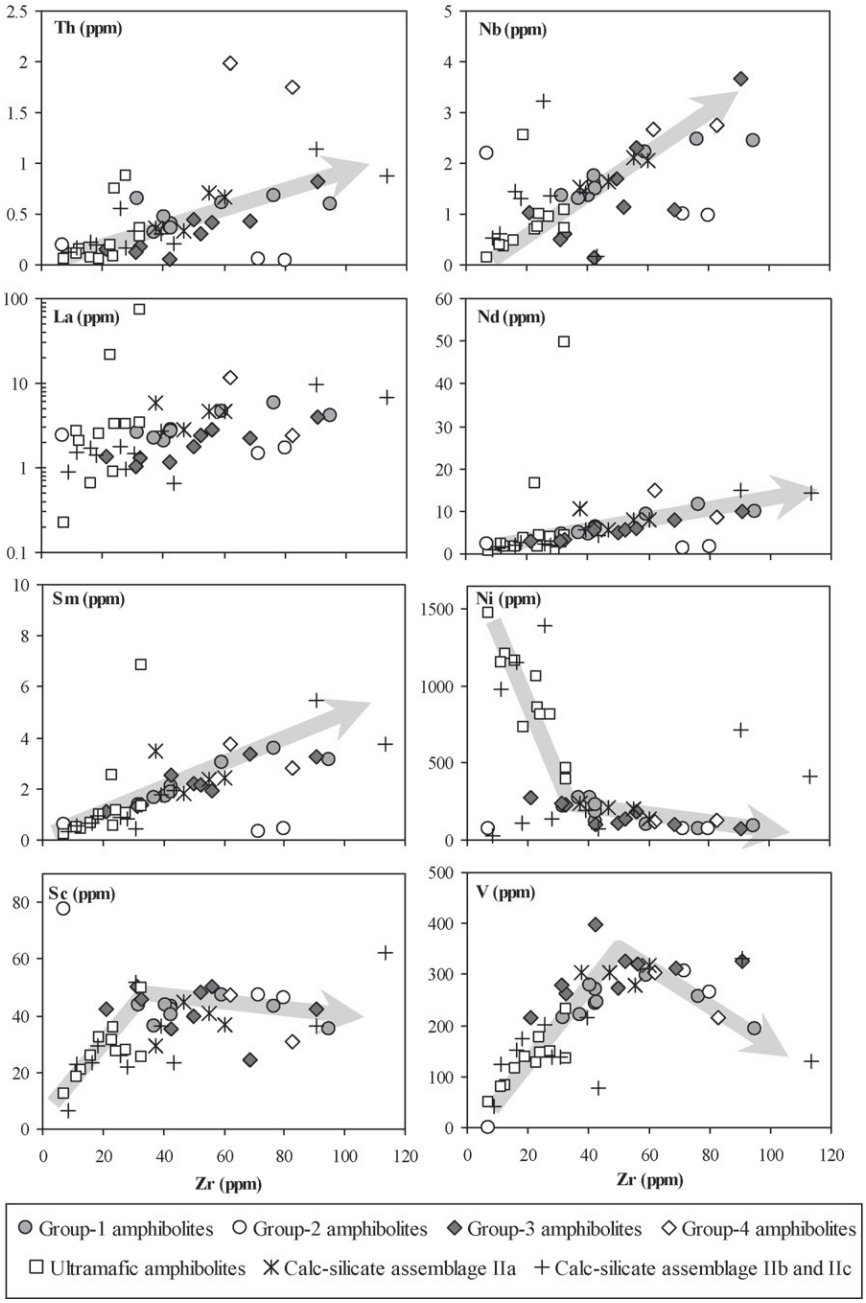

Fig. 7. Variation diagrams of Zr versus selected REE, HFSE, and transition metals. Ultramafic amphibolites from Polat et al. (2008) and this study (Table 2). Differentiation trends are indicated by arrows. The trace element variations of amphibolites are consistent with an ultramafic to mafic protolith. The stage-II calc-silicate rocks overlap the compositional trend of the amphibolites.

explained in terms of allochthonous terranes docked by horizontal lithospheric motions comparable to those of Phanerozoic collisional and accretionary orogens (Bridgwater et al., 1974; Friend et al., 1987, 1988, 1996; Nutman et al., 1989, 1993; McGregor et al., 1991; Polat et al., 2002; Polat and Hofmann, 2003; Friend and Nutman, 2005; Nutman, 2006). On the basis of field relations and geochemical characteristics, Polat et al. (2007a) suggested that the Ivisaartoq belt formed in a juvenile intra-oceanic island arc setting. The amphibolite-facies regional metamorphism recorded by the Ivisaartoq greenstone belt might have taken place during the terrane accretion, possibly during the docking of the Mesoarchean Kapisilik (*ca.* 3000 Ma) and Paleoarchean Isukasia (>3600 Ma) terranes, shortly before the intrusion of the weakly deformed *ca.* 2.960 Ma marginal granites (see Friend and Nutman, 2005).

The stage-II calc-silicate rocks are the products of prolonged metasomatic reactions. They provide evidence for changing physical and chemical conditions during metamorphism. For example, the replacement of the epidote-rich metasomatic assemblage IIa by the anhydrous garnet-clinopyroxene assemblage IIb indicates an increase in temperature. Metasomatic garnet and clinopyroxene replacing mineral assemblages in metasediments, metabasalts, komatiites, and iron formations have been documented to be formed at relatively high-*T* and

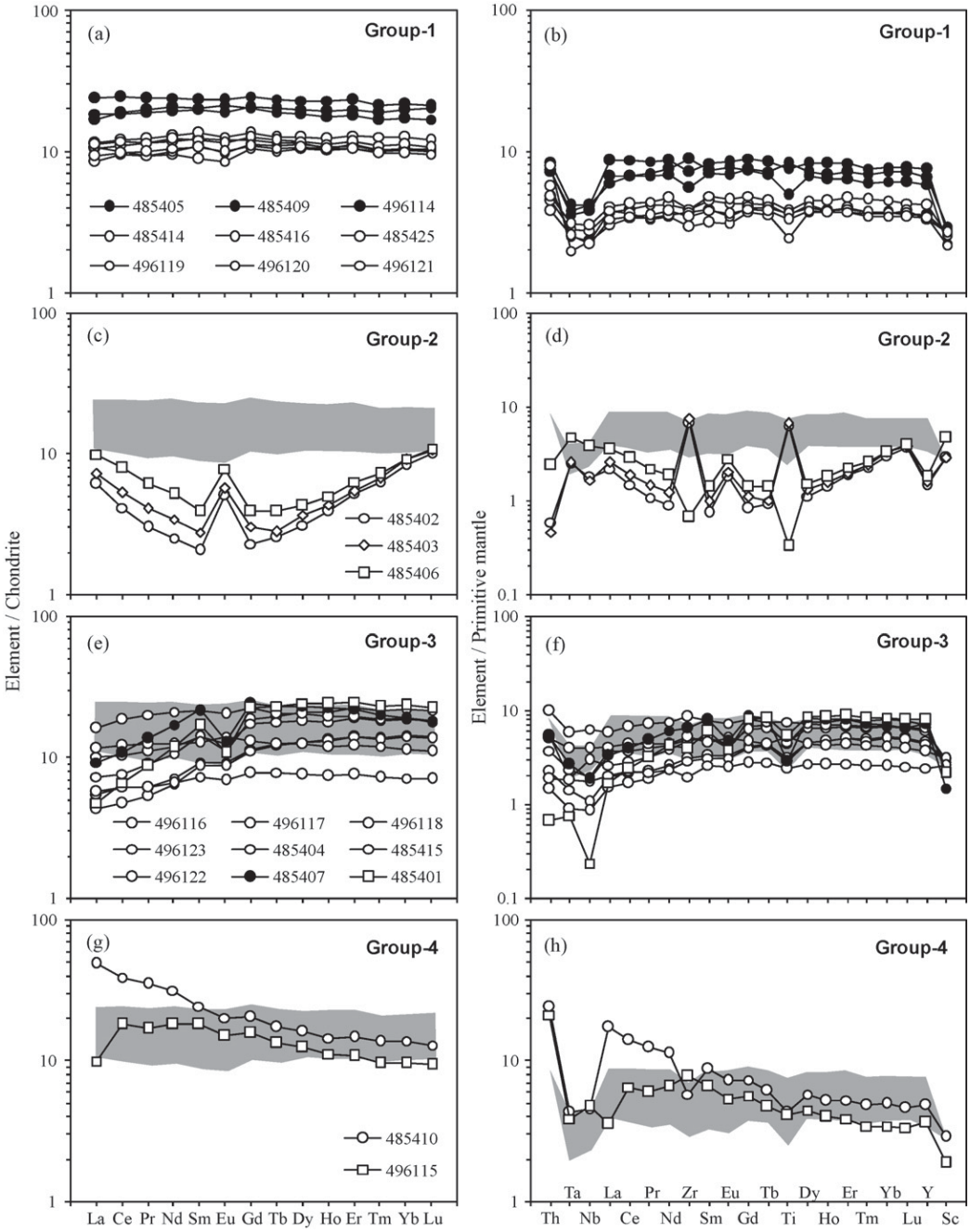

Fig. 8. Chondrite- and primitive mantle-normalized diagrams showing different groups of mafic amphibolites. The compositional field of Group 1 amphibolites (shaded area) is overlap to Groups 2–4 amphibolites for intercomparisons. Chondrite normalization values from Sun and McDonough (1989), and primitive mantle normalization values from Hofmann (1988).

intermediate-*P* (600–700 °C and 4.0–6.0 kbar ~ 12–18 km) during regional and/or contact metamorphism (e.g., Raith, 1991; Pan and Fleet, 1992; Mueller et al., 2004). The occurrence of garnet-diopside assemblage associated with ductile structures such as shear zones, tectonic boudins, and mylonitic foliations indicate that this assemblage was formed during the prograde stage of the regional amphibolite-facies metamorphism. In contrast, the metasomatic assemblage IIc exhibits cataclastic textures reflecting transitional ductile to brittle conditions. This brittle deformation and cataclasis might have accompanied the retrograde metamorphic evolution of the Ivisaartoq belt, possibly under upper greenschists-facies as indicated by the presence of accessory chlorite, tremolite, and calcite.

Transformation of mafic and ultramafic rocks into calc-silicates requires significant fluid-rock interaction, mass transfer, and reactions with Ca-rich fluids (see Rose et al., 1996). Fluids in metamorphic environments can be magmatic, derived from devolatilization reactions, meteoric, and mixtures of those fluid types (Rosing and Rose, 1993; Oliver, 1996; Ferry and Gerdes, 1998). There are no stable isotope or fluid inclusion studies to unequivocally address the origin of the fluids responsible for the stage-II calc-silicate metasomatism of the Ivisaartoq belt.

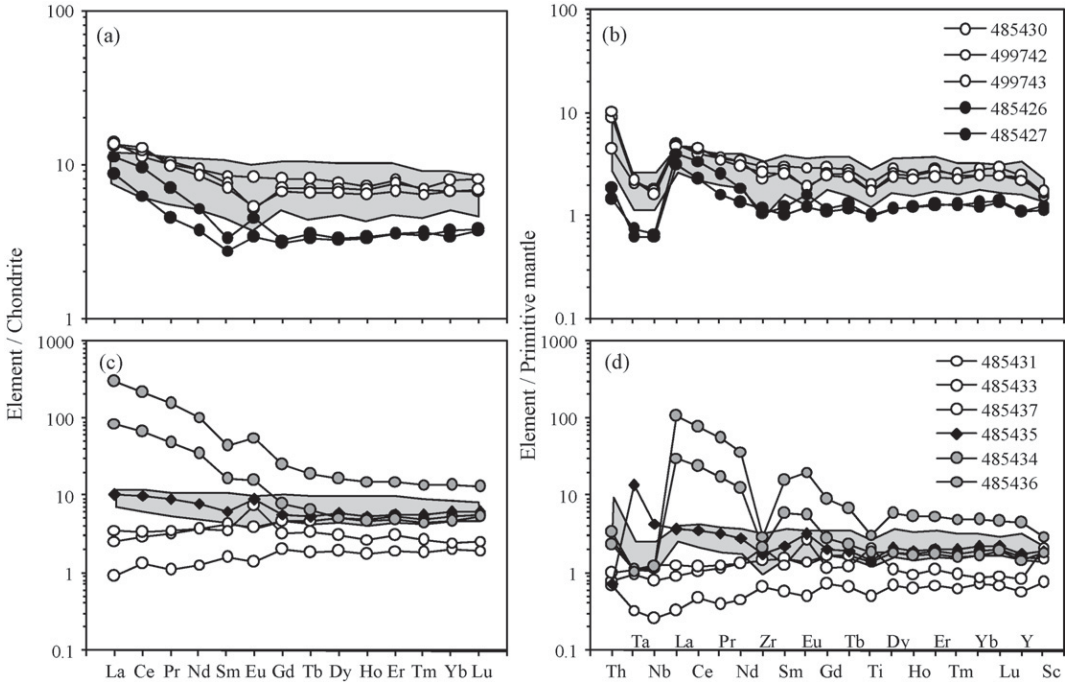

Fig. 9. Chondrite- and primitive mantle-normalized diagrams of ultramafic amphibolites. Samples 499742 and 499743 from this study (Table 2), other ultramafic amphibolites from Polat et al. (2008). The shaded area represents the composition of the least altered ultramafic pillows and cumulates of Polat et al. (2007a).

However, some constraints can be placed on the basis of field relationships. For instance, the contacts between the Ivisaartoq belt and the neighboring TTG-gneisses are marked by mylonites. Granites and granodiorites (*ca.* 2960 Ma) intruding the margins of the belt are only weakly deformed indicating that they post-date the regional metamorphism (Friend and Nutman, 2005). Granites and pegmatites occurring in the central parts of the belt transect the regional metamorphic fabrics and intrude the calc-silicate rocks. All these characteristics suggest that the intrusions exposed in the area are unlikely to be the source of metasomatic fluids. However, unexposed deep-seated syn-metamorphic intrusive rocks cannot be ruled out as the potential source of heat and fluids.

An alternative source of fluids could be metamorphic dehydration reactions. Fluids released during prograde metamorphism might have remobilized calcium from carbonates precipitated during sea-floor hydrothermal alteration in the sedimentary and volcanic rocks of the Ivisaartoq belt. Dehydration of clastic metasedimentary rocks in greenstone belts have been recognized as a significant source of fluids during regional meta-

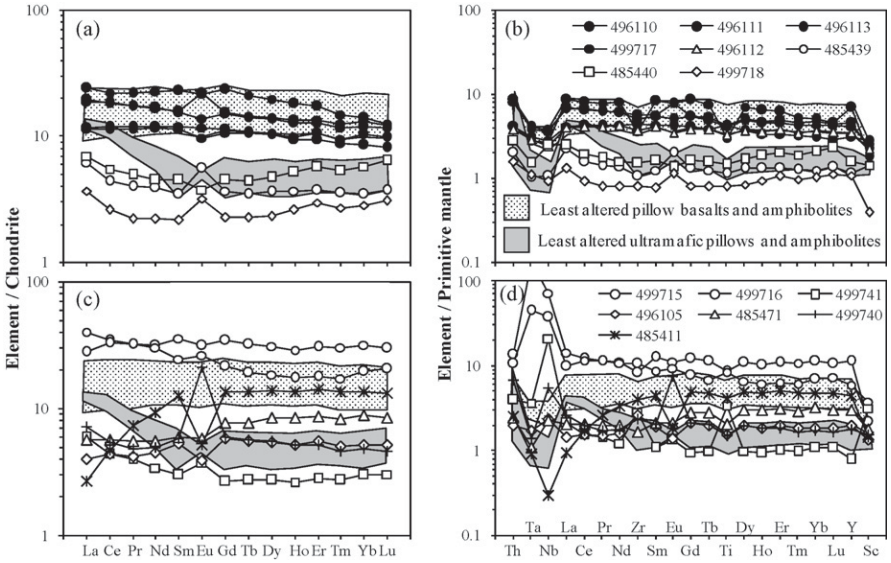

Fig. 10. Chondrite- and primitive mantle-normalized diagrams of stage-II calc-silicate rocks. Filled circles: samples with the metasomatic assemblage IIa; other symbols: samples variably overprinted by the metasomatic assemblages IIb and IIc. Fields of the least altered mafic and ultramafic rocks from Polat et al. (2007a,2008) and this study.

morphism, causing intense metasomatism and ore deposition in the mafic and ultramafic metavolcanic counterparts (cf. Van Hees et al., 1999; Shelton et al., 2004). The lowermost part of the Ivisaartoq belt comprises a 500 m thick clastic metasedimentary unit (Figs. 1 and 2) composed of quartz-feldspathic gneisses and pelitic schists. We speculate that this unit could have played an important role in the generation of fluids that reacted with mafic and ultramafic rocks to produce the prograde metasomatic assemblages IIa and IIb.

6.2. Element mobility during the stage-I metasomatic alteration

Polat et al. (2008) investigated the geochemical and Sm–Nd isotope characteristics of well preserved picritic to basaltic pillow lavas and ultramafic cumulate rocks of the upper amphibolite unit. These rocks display flat to slightly enriched REE patterns, negative anomalies of HFSE (mainly Nb–Ta), and positive initial ε_{Nd} (+0.30 to +4.97) values. The preservation of primary magmatic textures including relict igneous clinopyroxene, and the coherent geochemical and isotopic characteristics suggests that these rocks retain a near-primary magmatic composition (see Polat et al., 2008).

In addition, some basaltic pillow lavas from the upper amphibolite unit exhibit mineralogical and chemical zonation providing evidence for sea-floor hydrothermal alteration (Fig. 3(a and b)). Epidote-rich inner pillow cores appear to have resulted from reactions with fluids circulating through drainage cavities; whereas the amphibole-rich pillow rims most likely represent chloritized chilled margins owing to interaction with sea water (see Polat et al., 2007a). The outer pillow cores (Fig. 3(b)) appear to be an interface that remained relatively unaffected by sea-floor hydrothermal alteration. The average composition of these mineralogically and chemically zoned pillow basalts is presented in Table 2.

To assess the chemical changes that resulted from sea-floor alteration we present two isocon diagrams in Fig. 11. In the isocon method, the elemental concentrations of the precursor versus the altered counterpart are plotted to quantify mass changes and element mobility owing to metasomatism. Accordingly, immobile elements will plot along a straight line (isocon) intercepting the origin. The slope of this line quantifies the total mass change in the altered rocks. Gains and losses of mobile elements are indicated by their position either above or below the isocon line, respectively (see Gresens, 1967; Grant, 1986; Baumgartner and Olsen, 1995).

Relative to the least altered outer pillow cores, the isocon slopes (Fig. 11, Table 2) indicate a total mass gain of 3.6% in the inner pillow cores and a total mass loss of 5.5% in the pillow rims. The isocon diagrams confirm large mobility of major elements (Ca, K, Na, Fe, Mg), LILE (Pb, Rb, Cs, Ba), and LREE (mostly La, Ce, and Eu) in the inner cores and pillow rims. In contrast, HREE, Th, Nb, Ta, Zr, and Ti consistently plot along and close to the isocon lines indicating their relative immobile behaviour.

The outer pillow cores display flat to slightly enriched LREE, near-flat HREE, and Nb-depleted trace element patterns similar

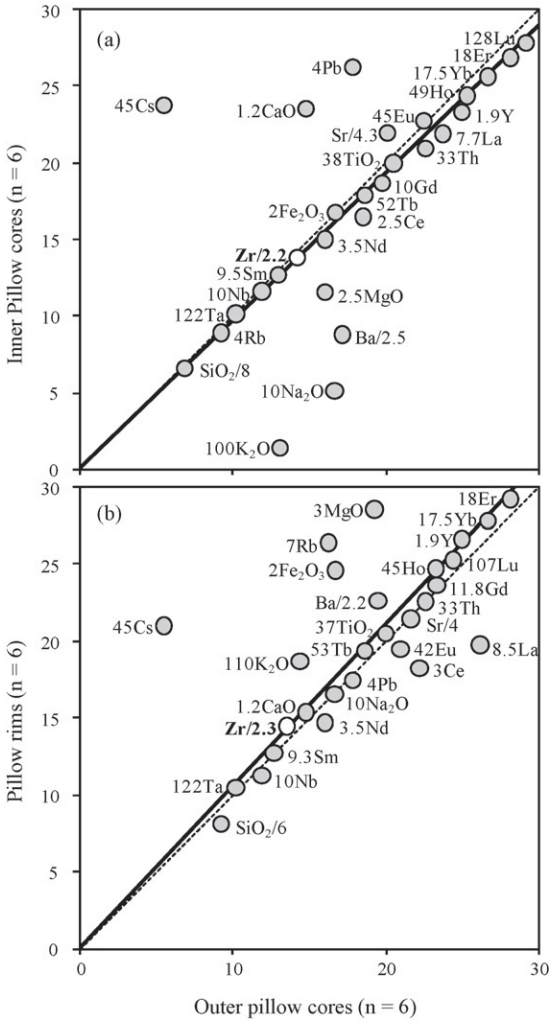

Fig. 11. Isocon diagrams of pillow basalts with core and rim structures resulting from stage-I calc-silicate alteration (see also Fig. 3(b)). Non-metasomatized outer pillow cores are compared with (a) strongly metasomatized inner pillow cores, and (b) amphibole-rich pillow rims. Sample compositions are average estimates from Polat et al. (2007a) (see Table 2). The isocon plots (solid lines) are defined using Zr as immobile element. Dashed line represents the line of constant mass (see Grant, 1986). Major elements are plotted in weigh percent and trace elements in ppm. Data are scaled as indicated.

to the least altered pillow basalts. These geochemical patterns have been interpreted as near-primary magmatic characteristics (Polat et al., 2007a).

6.3. Origin of the geochemical patterns in the metavolcanic rocks

The deformation of the pillow lavas increases towards the magnetic marker giving rise to amphibolites with penetrative foliation. Group 1 amphibolites exhibit similar trace element patterns (Fig. 8(a and b)) to those of the least altered pillow basalts suggesting that their REE and HFSE have not been significantly modified by the strong metasomatic alteration that affected the areas along the magnetic marker (Fig. 3(c–f)). Therefore, Group 1 amphibolites preserve near-primary geochemical characteristics.

The trace element patterns of Groups 2, 3, and 4 amphibolites are significantly different from those of the least altered pillow lavas (Fig. 8(c–h)). Several processes including source heterogeneity, crustal contamination, magma mixing, different degrees of partial melting, fractional crystallization, and hydrothermal alteration can produce the contrasting trace element patterns of these amphibolites. Therefore, they could represent either volcanic flows with contrasting petrogenesis, or their trace element patterns may reflect complex hydrothermal alteration of the pillow lavas.

The U-shape REE patterns of Group 2 amphibolites resemble those of Phanerozoic boninites (Fig. 8(c and d)). These REE patterns in boninites result from partial melting of strongly depleted refractory mantle that has been refertilized by subduction fluids or melts prior to, or during melt production (Hickey and Frey, 1982; Crawford et al., 1989; Falloon and Danyushevsky, 2000). Although secular variations of the earth mantle prevents strict comparisons with modern magmatism (e.g., Glikson, 2001), the petrogenesis of Archean boninite-like melts, like their modern counterparts, requires a mantle source that has been depleted through several partial melting events prior to boninitic volcanism (Smithies et al., 2004). Melting of a refractory source would result in high-Mg (4.0–22 wt.%) magmas with low TiO_2 (<0.5 wt.%) and Zr (<55 ppm) contents, and high concentrations of transition metals (Ni ~ 47–520 ppm; Cr > 196–2343 ppm) (cf. Smithies, 2002; Smithies et al., 2004, and references therein). In comparison to modern boninitic lavas, the Mesoarchean Ivisaartoq Group 2 amphibolites display higher contents of TiO_2 (up to 1.4 wt.%) and Zr (up to 80 ppm), and lower abundances of MgO (10–11 wt.%), Ni (71–75 ppm), and Cr (116–196 ppm), implying that Group 2 amphibolites are not metamorphosed boninitic lavas. In addition, these amphibolites display strong positive Eu anomalies (Fig. 8(c)). Accordingly, we suggest that the geochemical characteristics of Group 2 amphibolites reflect the mobility of many major and trace elements, including LILE, REE, and HFSE during post-magmatic metasomatic alteration. The concentrations of Ti and Zr in samples 485402 and 485403 are comparable to those of Group 1 amphibolites and least altered pillow basalts, indicating that they were derived from pillow basalt protoliths occurring in the upper volcanic sequence (upper amphibolites). Significant loss of the MREE, relative to Ti and Zr, would explain the U-shape REE patterns and the pronounced positive Ti and Zr anomalies of these samples (Fig. 8(c and d)). In contrast, sample 485406 displays strong negative Ti and Zr anomalies suggesting that these elements were locally remobilized along with the REE.

The flat HREE and depleted LREE patterns of Group 3 amphibolites resemble N-MORB (Fig. 8(e and f)). Unlike MORB, however, these amphibolites present negative Nb–Ta anomalies in primitive mantle-normalized diagrams. Crustal contamination and mixing with felsic magmas can result in negative HFSE anomalies and produce the enrichment of LREE from Group 3 to Groups 1 and 4 amphibolites. However, given the low concentration of transition metals (e.g., Ni, Co, and Cr) and MgO in felsic rocks, these processes would significantly decrease the content of these elements. In contrast, the concentration of transition metals and MgO of all amphibolite groups is comparable at a given Zr content (Figs. 6 and 7). Compelling evidence against significant crustal contamination and mixing in the petrogenesis of the Ivisaartoq volcanic rocks is provided by positive ε_{Nd} values of the associated mafic (+0.30 to +3.1) and ultramafic (+4.2 to +5.0) lavas (Polat et al., 2008).

Polat et al. (2007a) suggested that the Ivisaartoq belt formed in a suprasubduction zone. Basaltic rocks formed across those settings display complex trace element variations ranging from MORB-like REE patterns with negative Nb anomalies to typical arc lavas enriched in LREE and negative HFSE anomalies. These contrasting trace element patterns stem from different degrees of melting of heterogeneous depleted-mantle sources variably modified by subduction components (Klein and Karsten, 1995; Karsten et al., 1996; Sinton et al., 2003; Godard et al., 2006). Accordingly, these complex processes may well produce the negative Nb–Ta anomalies and the enrichment of LREE from Groups 3 to Groups 1 and 4 amphibolites. However, these processes would also result in lavas with distinct contents of MgO, transition metals, Zr, TiO_2, Y, and HREE reflecting the degree of melting and depletion of the sources. In contrast, the concentration of those elements in Groups 1, 3 and 4 amphibolites is virtually the same at a given Zr content (Figs. 6–8).

In addition, crystal fractionation of a parental magma cannot explain the crossed LREE patterns between different amphibolite groups. Even within Group 3 amphibolites, some samples (e.g., 485407 and 485401) display extremely low La/Sm_{cn} ratios and strong depletion of Nb despite their high HREE content (Fig. 8(e and f)). These patterns cannot be explained by fractionation but suggest that the LREE and Nb were remobilized.

Although melting of a heterogeneous mantle source could have played a major role in the formation of diverse geochemical compositions in the Ivisaartoq volcanic rocks, the evidence for significant element mobility in the vicinity of calc-silicate formations indicates that the large geochemical variations in the belt have resulted from post-magmatic alteration processes (Fig. 3(c–f)). In addition, all groups of amphibolites locally occur within the same outcrops (e.g., samples 485401, 485402, 405405, and 485410) without structural discontinuity. This suggests that their contrasting trace element patterns most likely resulted from alteration of the pillow basalts.

The ultramafic amphibolites provide additional evidence for significant post-magmatic alteration. For example, some ultramafic rocks, 485434 ($\varepsilon_{Nd} = +8.3$; $La/Yb_{cn} = 20$) and 485436 ($\varepsilon_{Nd} = +9.5$; $La/Yb_{cn} = 24$), display highly enriched LREE patterns (Fig. 9(c and d)) and strong positive ε_{Nd} values (see Polat et al., 2008). These samples are from the same outcrop as sample 485435 ($\varepsilon_{Nd} = +2.9$; $La/Yb_{cn} = 1.8$). Enrichment of LREE by crustal contamination cannot explain the more positive ε_{Nd} values. These contrasting geochemical variations have been attributed to post-magmatic alteration (Polat et al., 2008). Altered ultramafic rocks display slightly depleted to extremely enriched LREE patterns and variable negative to positive anomalies of Eu, Nb, Ta, Ti, and Zr (Fig. 9(c and d)). In contrast, some samples still preserve geochemical characteristics comparable to the least altered ultramafic pillows and cumulates (Fig. 9(a and b)) (Polat et al., 2007a). They possess slight LREE-enriched patterns and consistent negative anomalies of HFSE (especially Nb

and Ta). We interpret these rocks as the least altered ultramafic amphibolites.

On variation diagrams, Zr is used as an alteration and differentiation index (Figs. 6 and 7) because of its immobile behaviour in different geological conditions, and consistent incompatibility during fractionation of ultramafic to mafic magmas (Winchester and Floyd, 1977; Barrett and MacLean, 1994; Pearce, 1996). Accordingly, immobile elements will display systematic correlations with Zr consistent with magmatic fractionation. Some major elements such as Si, Mg, Ca, Fe, Na, K, and trace elements including Rb, Sr, Ba, Pb show no correlation on variation diagrams indicating large mobility in all amphibolites (Figs. 6 and 7). Scatter of REE, Ti, Th, Nb, and Y on variation diagrams is consistent with various degrees of mobility of these elements. Transition metals Ni, V, Sc, Co, and Cr present excellent correlation with Zr (Fig. 7) in all amphibolites indicating that these elements were practically immobile during alteration.

Despite element mobility, systematic trends of increasing Al, REE, and HFSE with increasing Zr can be resolved. These trends are shared by all amphibolites. It is unlikely that the linear trends on variation diagrams of Zr represent a liquid line of descent given the differences in ε_{Nd} values between ultramafic and mafic pillows. However, the collective geochemical correlations suggest crystal fractionation. For example, ultramafic rocks exhibit a steep negative correlation of Ni versus Zr consistent with olivine fractionation (Fig. 7). Aluminum content increases with increasing Zr in ultramafic amphibolites but decreases in the mafic amphibolites suggesting that plagioclase was only important during fractionation of the basaltic melts (Fig. 6). The trends of Sc and V reflect clinopyroxene fractionation. Fractionation of these mineral phases is consistent with the occurrence of olivine-bearing ultramafic sheets grading upwards into gabbroic rocks, clinopyroxene-rich cumulates, anorthosites intrusions, and plagioclase-rich ocelli structures in gabbros and basalts.

There is no unequivocal evidence indicating the relative timing of this alteration. However, the samples in this study were collected along a high strain zone at the contact between the upper and lower amphibolite groups. This zone was a fluid pathway during the regional metamorphism as indicated by ductile calc-silicate layers, quartz veins, and silicic mylonites (Section 6.1). We postulate that the alteration patterns displayed by Groups 2–4 amphibolites were formed during the regional metamorphic event coeval with the stage-II calc-silicate metasomatism.

6.4. Element mobility during the stage-II calc-silicate metasomatism

The stage-II calc-silicate rocks resulted from prolonged metasomatic reactions in ultramafic to mafic rocks. Local mobility of REE and HFSE in the magmatic precursors makes a quantitative estimation of elemental mass changes difficult because most methods use ratios of immobile elements as a datum (Gresens, 1967; Grant, 1986; MacLean and Kranidiotis, 1987; MacLean, 1988, 1990). Thus, we present a qualitative evaluation of the chemical changes occurring during the stage-II calc-silicate metasomatism.

As a group, the stage-II calc-silicate rocks represent significant additions of Ca and losses of Na and K relative to the volcanic protoliths (Fig. 6). Manganese, Fe, and Mg, were consistently lost during formation of the prograde assemblage IIa, and gained to form the garnet-clinopyroxene metasomatic assemblage IIb. Some LILE such as Rb, Sr, Ba, and Pb were variably enriched in the calc-silicate assemblages IIb and IIc.

Primitive mantle- and chondrite-normalized trace element patterns of the stage-IIa calc-silicates are slightly depleted in HREE, however, the concentration levels of trace elements are comparable to those of the least altered mafic amphibolites and pillow basalts (filled symbols, Fig. 10(a and b)). Moreover, the concentrations of Ni, Sc, V, Cr, and Co in this assemblage are consistent with a basaltic protolith (Fig. 7). These characteristics indicate that Th, Nb, Ta, Ti, Zr, REE (excepting Eu), and transition metals were not significantly changed during the development of the metasomatic assemblage IIa.

Large additions of Ca (CaO = 17–30 vs. 15–22 wt.% in the assemblage IIa) in calc-silicate assemblages IIb and IIc resulted in low REE and HFSE abundances (<3× primitive mantle values) due to residual dilution (Fig. 10). For instance, sample 499718 (CaO ~ 30 wt.%) exhibits low concentrations of transition metals (e.g., Ni = 29; Cr = 47, and Co = 11 ppm) coupled with low REE and HFSE contents (Fig. 10(a and b)). However, low trace element abundances in some calc-silicates may reflect the composition of their protoliths. Samples 499740 and 499741 were collected from calc-silicate boudins spatially associated with ultramafic amphibolites (see Fig. 3(d)). They display high Ni (>1300 ppm), Co (>100 ppm), and Cr (>1500 ppm) contents, and low abundances of REE and HFSE consistent with an ultramafic precursor (Fig. 10(c and d)).

The stages-IIb and -IIc calc-silicate rocks exhibit evidence for REE and HFSE mobility. Sample 485411 (Fig. 10(c and d)) displays a strongly depleted LREE pattern similar to those of Group 3 amphibolites (Fig. 8(e and f)) suggesting loss of LREE. Gains and losses of HFSE are indicated by strong positive (samples 499715, 499716, and 499741) and complementary large negative (sample 485411) Nb–Ta anomalies in primitive mantle-normalized diagrams (Fig. 10(d)). Despite strong Ca enrichment, samples 499715 and 499716 posses high REE contents. This suggests that REE were enriched in these samples.

Retrograde overprinting makes it difficult to determine whether the REE, Nb, and Ta were mobilized during the development of the metasomatic assemblage IIb or the retrograde assemblage IIc. Calc-silicate metasomatism of volcanic rocks in other Archean greenstone belts has resulted in significant mobility of the REE and HFSE mainly during the formation of prograde garnet-pyroxene assemblages (e.g., Galley et al., 2000). In addition, experimental and empirical studies indicate that HFSE are more easily mobilized at high temperatures (cf. Rubin et al., 1993; Van Baalen, 1993; Tilley and Eggleton, 2005; Wood, 2005). Therefore, we suggest that the observed remobilization of HFSE and REE may have occurred during the formation of garnet-clinopyroxene assemblage IIb, probably over 500 °C.

7. Conclusions and implications

Geochemical investigations of Archean volcanic rocks, as a proxy to understand the magmatic and tectonic evolution of greenstone belts, rely on the systematics of elements that are not easily disturbed during hydrothermal alteration and metamorphism. Most major elements (Si, Na, K, Ca, Mg, and Fe) and LILE (Rb, Cs, Ba, Sr, Pb, U) are highly mobile during fluid-rock interaction limiting their use in petrologic and tectonic investigations (Hart et al., 1974; Condie et al., 1977; Ludden and Thompson, 1979; Ludden et al., 1982; Ague, 1994; Staudigel et al., 1996; Alt, 1999; Masters and Ague, 2005). In contrast, transition metals (Ni, Sc, Co, Cr, and V), HFSE (Zr, Ti, Nb, Ta, and Th), and REE (mainly the HREE) have been reliably used to investigate the evolution of variably altered and metamorphosed greenstone belts due to their largely immobile behaviour (Arndt, 1994; Polat and Hofmann, 2003; Polat et al., 2003).

This study has provided evidence for remobilization of those (e.g., REE and HFSE) normally immobile trace elements during a second stage of calc-silicate metasomatism yielding the following results:

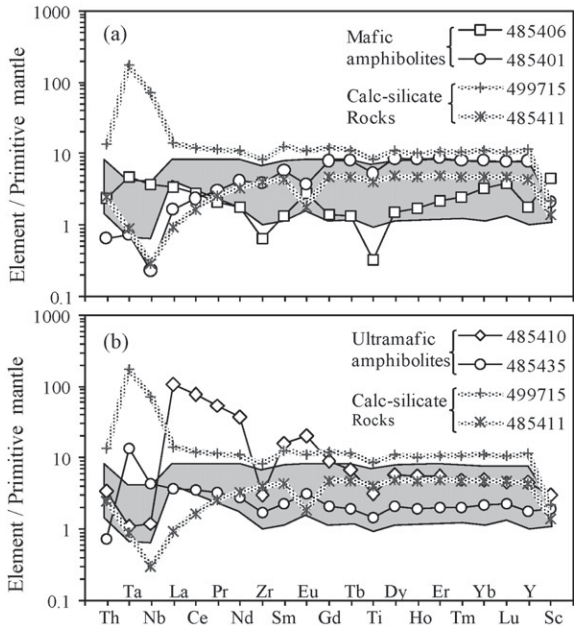

Fig. 12. Summary of the geochemical patterns displayed by mafic (a) and ultramafic (b) amphibolites and associated stage-II calc-silicates. Shaded area represents the composition of least altered mafic and ultramafic metavolcanic rocks of the Ivisaartoq belt (from Polat et al., 2007a,2008; this study).

1. Although almost all normally 'immobile' elements were disturbed, the collective geochemical correlations with Zr suggest different degrees of mobility. Accordingly, trace element mobility in the stage-II calc-silicate rocks and associated amphibolites increases from Zr, Ti, Ni, V, and Co, through HREE, Th, Nb, Ta, Y, Al, Sc, and Cr, to LREE and MREE. Petrographic and geochemical characteristics of calc-silicate rocks appear to indicate that the mobility of HFSE and REE occurred during the prograde stage of the regional metamorphism at upper amphibolite-facies conditions (stage-II metasomatism). This trace element mobility contrasts with the consistent immobile behaviour of HREE and HFSE during an early stage of sea-floor hydrothermal alteration (stage-I metasomatism).
2. Altered amphibolites and calc-silicate rocks exhibit complementary trace element patterns of enriched and depleted LREE, Th, Nb, and Ta (Fig. 12). It is noteworthy that the mobility of these elements occurred along shear zones and resulted in the formation of amphibolites with trace element characteristics resembling those displayed by volcanic rocks formed at contrasting tectonic settings such as boninites and N-MORB-like lavas (cf. Dostal et al., 1980). Considering these trace element patterns as primary can lead to misleading geodynamic interpretations.
3. The close spatial association of strongly altered and least altered metavolcanic rocks indicates that the REE and HFSE (mainly Th, Nb and Ta) were mobile on a local scale (1–4 m). It appears that the REE were removed at some localities, giving rise to Groups 2 and 3 amphibolites, and re-precipitated within several meters, generating the LREE-enriched patterns of Group 4 amphibolites and some ultramafic rocks (Figs. 8 and 9).
4. Despite large element mobility, mafic and ultramafic amphibolites display discernable linear trends on diagrams of Zr versus REE, HFSE, and transition metals (Figs. 6 and 7). Net gains or losses of major elements during hydrothermal alteration (e.g., silicification, chloritization, calc-silicate alteration, etc.) may well produce positive linear trends of immobile elements due to residual dilution or enrichment effects (Finlow-Bates and Stumpfl, 1981; MacLean and Kranidiotis, 1987; MacLean, 1990; MacLean and Hoy, 1991; Barrett and MacLean, 1994; Ague, 1994). Although Ca, Mg, Fe, and Si were mobile during post-magmatic alteration, the abundance of these elements in the Ivisaartoq amphibolites is still consistent with basaltic to picritic compositions (see also Polat et al., 2007a). This suggests that alteration and metamorphism did not produce significant mass changes, except where intense calc-silicate replacement occurred. Therefore, the correlation of REE, HFSE, and transition metals with Zr resulted from magmatic processes.
5. Near-primary magmatic signatures in the amphibolites are indicated by inflections on variation diagrams (e.g., Zr versus Al, Ni, Sc, and V) which are more likely produced by magmatic fractionation (Figs. 6 and 7). Although differences in ε_{Nd} values between mafic and ultramafic pillows and cumulates rule out a parental magma (Polat et al., 2008), taken all together, the covariations of transition metals and Al with Zr indicate fractionation of olivine, clinopyroxene, and plagioclase.
6. The geochemical characteristics of the Ivisaartoq volcanic rocks indicate that they are part of the same mafic to ultramafic volcanic suite. The least altered Group 1 amphibolites and ultramafic rocks (Figs. 8(a and b) and 9(a and b)) exhibit trace element patterns with flat to slightly enriched LREE, consistent negative Nb–Ta anomalies, and flat-HREE. These

geochemical characteristics are consistent with subduction zone geochemical signatures (see Hawkesworth et al., 1993; Pearce and Peate, 1995) and partial melting of a garnet-free shallow mantle source region.

Acknowledgements

We thank Z. Yang, and J.C. Barrette for their help during the ICP-MS analyses. This is a contribution of PREA and NSERC grant 250926 to A. Polat, and NSERC grant 83117 to B. Fryer. Field worked was funded by the Bureau of Minerals and Petroleum in Nuuk and the Geological Survey of Denmark and Greenland (GEUS). Two anonymous reviewers are thanked for providing excellent critiques and constructive comments on an early version of this paper which resulted in significant improvement of this study.

References

Ague, J.J., 1994. Mass transfer during Barrovian metamorphism of pelites, south-central Connecticut. I: Evidence for changes in composition and volume. Am. J. Sci. 294, 989–1057.

Alt, J.C., 1999. Hydrothermal alteration and mineralization of oceanic crust: mineralogy, geochemistry, and processes. In: Barrie, C.T., Hannington, M.D. (Eds.), Volcanic-associated Massive Sulphide Deposits: Processes and Examples in Modern and Ancient Settings. Rev. Econ. Geol. 8, 133–155.

Appel, P.W.A., 1983. Tungsten in the Godthåb area, West Greenland. Rapport Grønlands Geologiske Undersøgelse 1115, 59–64.

Appel, P.W.A., 1994. Stratabound scheelite in altered Archean komatiites, West Greenland. Mineralium Deposita 29, 341–352.

Appel, P.W.A., 1997. High bromine contents and low Cl/Br ratios in hydrothermally altered Archean komatiitic rocks, West Greenland. Precambrian Res. 82, 177–189.

Arndt, N.T., 1994. Archean komatiites. In: Condie, K.C. (Ed). Archean Crustal Evolution. Dev. Precambrian Geol. 11, 11–44.

Barrett, T.J., MacLean, W.H., 1994. Chemostratigraphy and hydrothermal alteration in exploration for VHMS deposits in greenstones and younger volcanic rocks. In: Lentz, D.R. (Ed.). Alteration and Alteration Processes Associated with Ore-forming Systems. Geol. Assoc. Can., Short Course Notes 11, 433–467.

Baumgartner, L.P., Olsen, S.N., 1995. A least-squares approach to mass transport calculations using the isocon method. Econ. Geol. 90, 1261–1270.

Brewer, M., Chadwick, B., Coe, K., Park, J.F.W., 1984. Further field observations in the Ivisârtoq Region of southern West Greenland. Rapport Grønlands Geologiske Undersøgelse 120, 55–67.

Bridgwater, D., McGregor, V.R., Myers, J.S., 1974. A horizontal tectonic regime in the Archean of Greenland and its implications for early crustal thickening. Precambrian Res. 1, 179–197.

Chadwick, B., 1985. Contrasting styles of tectonism and magmatism in the late Archaean crustal evolution of the northeastern part of the Ivisârtoq region, inner Godthåbsfjord, southern West Greenland. Precambrian Res. 27, 215–238.

Chadwick, B., 1986. Malene stratigraphy and late Archean structure: new data from Ivisaartoq, inner Godthåbsfjord, southern West Greenland. Rapport Grønlands Geologiske Undersøgelse 130, 74–85.

Chadwick, B., 1990. The stratigraphy of supracrustal rocks within high-grade orthogneisses and its bearing on Late Archean structure in southern West Greenland. J. Geol. Soc. London 147, 639–652.

Chadwick, B., Coe, K., 1988. Geological map of Greenland, 1:100,000, Ivisaartoq sheet 64 V. Nord. Copenhagen, Geological Survey of Greenland.

Condie, K.C., Viljoen, M.J., Kable, E.J.D., 1977. Effects of alteration on element distributions in Archean tholeiites from the Barberton greenstone belt, South Africa. Contrib. Mineral. Petrol. 64, 75–89.

Crawford, A.J., Falloon, T.J., Green, D.H., 1989. Classification, petrogenesis and tectonic setting of boninites. In: Crawford, A.J. (Ed.), Boninites and Related Rocks. Unwin-Hyman, London, pp. 1–49.

Dostal, J., Strong, D.F., Jamieson, R.A., 1980. Trace element mobility in the mylonite zone within the ophiolite aureole, St. Anthony Complex, Newfoundland. Earth Planet. Sci. Lett. 49, 188–192.

Falloon, T.J., Danyushevsky, L.V., 2000. Melting of refractory mantle at 1.5, 2 and 2.5 GPa under anhydrous and H_2O-undersaturated conditions: Implications for the petrogenesis of high-Ca boninites and the influence of subduction components on mantle melting. J. Petrol. 41 (2), 257–283.

Ferry, J.M., Gerdes, M.L., 1998. Chemically reactive fluid flow during metamorphism. Ann. Rev. Earth Planet. Sci. 26, 255–287.

Finlow-Bates, T., Stumpfl, E.F., 1981. The behavior of so called immobile elements in hydrothermally altered rocks associated with volcanogenic submarine-exhalative ore deposits. Mineralium Deposita 16, 319–328.

Friend, C.R.L., Nutman, A.P., 2005. New pieces to the Archaean terrane jigsaw puzzle in the Nuuk Region, southern West Greenland: Steps in transforming a simple insight into a complex regional tectonothermal model. J. Geol. Soc. London 162, 147–162.

Friend, C.R.L., Nutman, A.P., Baadsgaard, H., Kinny, P.D., McGregor, V.R., 1996. Timing of late Archean terrane assembly, crustal thickening and granite emplacement in the Nuuk region, southern West Greenland. Earth Planet. Sci. Lett. 142, 353–365.

Friend, C.R.L., Nutman, A.P., McGregor, V.R., 1987. Late-Archaean tectonics in the Færingehavn-Tre Brødre area, south of Buksefjorden, southern West Greenland. J. Geol. Soc. London 144, 369–376.

Friend, C.R.L., Nutman, A.P., McGregor, V.R., 1988. Late Archean terrane accretion in the Godthåb region, southern West Greenland. Nature 335, 535–538.

Fryer, B.J., Fyfe, W.S., Kerrich, R., 1979. Archean volcanogenic oceans. Chem. Geol. 24, 25–33.

Galley, A.G., Jonasson, I.R., Watkinson, D.H., 2000. Magnetite-rich calc-silicate alteration in relation to synvolcanic intrusions at the Ansil volcanogenic massive sulfide deposit, Rouyn-Noranda, Quebec, Canada. Mineralium Deposita 35, 619–637.

Garde, A.A., 2007. A mid-Archean Island arc complex in the Eastern Akia terrane, Godthåbsfjord, southern West Greenland. J. Geol. Soc. London 164, 565–579.

Gélinas, L., Mellinger, M., Trudel, P., 1982. Archean mafic metavolcanics from the Rouyn-Noranda district, Abitibi Greenstone Belt, Quebec. 1. Mobility of the major elements. Can. J. Earth Sci. 19, 2258–2275.

Glikson, A.Y., 2001. The astronomical connection of terrestrial evolution: crustal effects of post-3.8 Ga mega-impact clusters and evidence for major 3.2 ± 0.1 Ga bombardment of the Earth–Moon system. J. Geodyn. 32, 205–229.

Godard, M., Bosch, D., Einaudi, F., 2006. A MORB source for low-Ti magmatism in the Semail ophiolite. Chem. Geol. 234 (1–2), 58–78.

Grant, J.A., 1986. The isocon diagram—a simple solution to Gresens' equation for metasomatic alteration. Econ. Geol. 81, 1976–1982.

Gresens, R.L., 1967. Composition–volume relationships of metasomatism. Chem. Geol. 2, 47–65.

Gruau, G., Rosing, M., Bridgwater, D., Gill, R.C.O., 1996. Resetting of Sm–Nd systematics during metamorphism of >3.7-Ga rocks: implications for isotopic models of early Earth differentiation. Chem. Geol. 133, 225–240.

Gruau, G., Tourpin, S., Fourcade, S., Blais, S., 1992. Loss of isotopic (Nd, O) and chemical (REE) memory during metamorphism of komatiites: new evidence from eastern Finland. Contrib. Mineral. Petrol. 112, 66–82.

Hart, S.R., Erlank, A.J., Kable, E.J.D., 1974. Sea-floor basalt alteration: Some chemical and isotopic effects. Contrib. Mineral. Petrol. 44, 219–230.

Hawkesworth, C.J., Gallanger, K., Hergt, J.M., McDetmott, F., 1993. Mantle and slab contributions in arc magmas. Ann. Rev. Earth Planet. Sci. 21, 175–204.

Hall, R.P., 1980. The tholeiitic and komatiitic affinity of Malene metavolcanic amphibolites from Ivisaartoq, southern West Greenland. Rapport Grønlands Geologiske Undersøgelse 97, 20 pp.

Hall, R.P., Friend, C.R.L., 1979. Structural evolution of the Archean rocks in Ivisârtoq and the neighboring inner Godthåbsfjord region, southern West Greenland. Geology 7, 311–315.

Hickey, R.L., Frey, F.A., 1982. Geochemical characteristics of boninitic series volcanics: implications for their source. Geochim. Cosmochim. Acta 46, 2099–2115.

Hofmann, A.W., 1988. Chemical differentiation of the Earth: the relationship between mantle, continental crust, and oceanic crust. Earth Planet. Sci. Lett. 90, 297–314.

Jenner, G.A., Longerich, H.P., Jackson, S.E., Fryer, B.J., 1990. ICP-MS; a powerful tool for high-precision trace-element analysis in earth sciences; evidence from analysis of selected U.S.G.S. Reference samples. Chem. Geol. 83, 133–148.

Karsten, J.L., Klein, E.M., Sherman, S.B., 1996. Subduction zone geochemical characteristics in ocean ridge basalts from the southern Chile Ridge: implications of modern ridge subduction systems for the Archean. Lithos 37 (2–3), 143–161.

Klein, E.M., Karsten, J.L., 1995. Ocean-ridge basalts with convergent-margin geochemical affinities from the Chile Ridge. Nature 374, 52–57.

Lahaye, Y., Arndt, N.T., Byerly, G., Chauvel, C., Fourcade, S., Gruau, G., 1995. The influence of alteration on the trace-element and Nd isotopic compositions of komatiites. Chem. Geol. 126, 43–64.

Ludden, J.N., Gelinas, L., Trudel, P., 1982. Archean metavolcanics from the Rouyn-Noranda district, Abitibi greenstone belt, Quebec. 2. Mobility of trace elements and petrogenetic constraints. Can. J. Earth Sci. 19, 2276–2287.

Ludden, J.N., Thompson, G., 1979. An evaluation of the behavior of the rare earth elements during the weathering of sea-floor basalts. Earth Planet. Sci. Lett. 43, 85–92.

MacLean, W.H., 1988. Rare earth element mobility at constant inter-REE ratios in the alteration zone at the Phelps Dodge massive sulphide deposit, Matagami, Quebec. Mineralium Deposita 23, 231–238.

MacLean, W.H., 1990. Mass change calculations in altered rocks series. Mineralium Deposita 25, 1–6.

MacLean, W.H., Hoy, L.D., 1991. Geochemistry of hydrothermally altered rocks at the Horn mine, Noranda, Quebec. Econ. Geol. 86, 506–528.

MacLean, W.H., Kranidiotis, P., 1987. Immobile elements as monitors of mass transfer in hydrothermal alteration: Phelps Dodge massive sulfide deposit, Matagami, Quebec. Econ. Geol. 82, 951–962.

McGregor, V.R., Friend, C.R.L., Nutman, A.P., 1991. The late Archean mobile belt through the Godthåbsfjord, southern West Greenland; a continent-continent collision zone? Bull. Geol. Soc. Denmark 39, 179–197.

Masters, R.L., Ague, J.J., 2005. Regional-scale fluid flow and element mobility in Barrow's metamorphic zones, Stonehaven, Scotland. Contrib. Mineral. Petrol. 150, 1–18.

Middelburg, J.J., Van der Weijden, C.H., Woittiez, J.R.W., 1988. Chemical processes affecting the mobility of major, minor and trace elements during weathering of granitic rocks. Chem. Geol. 68 (3–4), 253–273.

Mueller, A.G., Nemchin, A.A., Frei, R., 2004. The Nevoria Gold Skarn deposit, Southern Cross Greenstone Belt, Western Australia: II. Pressure–temperature–time path and relationship to postorogenic granites. Econ. Geol. 99, 453–478.

Nutman, A.P., 2006. Antiquity of the oceans and continents. Elements 2 (4), 223–227.

Nutman, A.P., Friend, C.R.L., Baadsgaard, H., McGregor, V.R., 1989. Evolution and assembly of Archean Gneiss Terranes in the Godthåbsfjord Region, Southern West Greenland: structural, metamorphic, and isotopic evidence. Tectonics 8 (3), 573–589.

Nutman, A.P., Friend, C.R.L., Kinny, P.D., McGregor, V.R., 1993. Anatomy of an early Archean gneiss complex: 3900–3600 Ma crustal evolution in southern West Greenland. Geology 21, 415–418.

Oliver, N.H.S., 1996. Review and classification of structural controls on fluid flow during regional metamorphism. J. Metamorphic Geol. 14, 477–492.

Pan, Y., Fleet, M.E., 1992. Mineralogy and genesis of calc-silicates associated with Archean volcanogenic massive sulphide deposits at the Manitouwadge mining camp, Ontario. Can. J. Earth Sci. 29, 1375–1388.

Pearce, J.A., 1996. A user's guide to basalt discrimination diagrams. In: Wyman, D.A. (Ed.). Trace Element Geochemistry of Volcanic Rocks: Applications for Massive Sulphide Exploration. Geological Association of Canada, GAC Short Course Notes 12, 79–113.

Pearce, J.A., Peate, D.W., 1995. Tectonic implications of the composition of volcanic arc magmas. Ann. Rev. Earth Planet. Sci. 23, 251–285.

Polat, A., Appel, P.W.U., Frei, R., Pan, Y., Dilek, Y., Ordóñez-Calderón, J.C., Fryer, B., Hollis, J.A., Raith, J.G., 2007a. Field and Geochemical Characteristics of the Mesoarchean (∼3075 Ma) Ivisaartoq greenstone belt, southern West Greenland: Evidence for sea floor hydrothermal alteration in suprasubduction oceanic crust. Gondwana Res. 11, 69–91.

Polat, A., Frei, R., Appel, P.W.U., Dilek, Y., Fryer, B., Ordóñez-Calderón, J.C., Yang, Z., 2008. The origin and compositions of Mesoarchean oceanic crust: Evidence from the 3075 Ma Ivisaartoq greenstone belt, SW Greenland. Lithos 100, 293–321.

Polat, A., Hofmann, A.W., 2003. Alteration and geochemical patterns in the 3.7–3.8 Ga Isua greenstone belt, West Greenland. Precambrian Res. 126, 197–218.

Polat, A., Hofmann, A.W., Münker, C., Regelous, M., Appel, P.W.U., 2003. Contrasting geochemical patterns in the 3.7–3.8 Ga pillow basalt cores and rims, Isua greenstone belt, Southwest Greenland: implications for post-magmatic alteration processes. Geochim. Cosmochim. Acta 67 (3), 441–457.

Polat, A., Hofmann, A.W., Rosing, M.T., 2002. Boninite-like volcanic rocks in the 3.7–3.8 Ga Isua greenstone belt, West Greenland: geochemical evidence for intra-oceanic subduction zone processes in the early Earth. Chem. Geol. 184, 231–254.

Raith, J.G., 1991. Stratabound tungsten mineralization in regional metamorphic calc-silicate rocks from the Australpine crystalline complex, Australia. Mineralium Deposita 26, 72–80.

Raith, J.G., Polat, A., Appel, P.W.U., 2006. Hydrothermal alteration of Archean oceanic crust in the Ivisaartoq greenstone belt, southern West Greenland. In: Pangeo Conference Series, Austria, pp. 264–265.

Rose, N.M., Rosing, M.T., Bridgwater, D., 1996. The origin of metacarbonate rocks in the Archaen Isua supracrustal belt, west Greenland. Am. J. Sci. 296, 1004–1044.

Rosing, M.T., Rose, N.M., 1993. The role of ultramafic rocks in regulating the concentrations of volatile and non-volatile components during deep crustal metamorphism. Chem. Geol. 108, 187–200.

Rubin, J.N., Henry, C.D., Price, J.G., 1993. The mobility of zirconium and other "immobile" elements during hydrothermal alteration. Chem. Geol. 110, 29–47.

Shelton, K.L., McMenamy, T.A., Van Hees, E.H.P., Falck, H., 2004. Deciphering the complex fluid history of a Greenstone–Hosted gold deposit: fluid inclusion and stable isotope studies of the Giant Mine, Yellowknife, Northwest Territories, Canada. Econ. Geol. 99, 1643–1663.

Sinton, J.M., Ford, L.L., Chappell, B., McCulloch, M.T., 2003. Magma genesis and mantle heterogeneity in the Manus back-arc basin, Papua New Guinea. J. Petrol. 44 (1), 159–195.

Smithies, R.H., 2002. Archean boninites-like rocks in an intracratonic setting. Earth Planet. Sci. Lett. 197, 19–34.

Smithies, R.H., Champion, D.C., Sun, S., 2004. The case for Archean boninites. Contrib. Mineral. Petrol. 147, 705–721.

Staudigel, H., Plank, T., White, B., Schmincke, H.-U., 1996. Geochemical fluxes during sea floor alteration of the basaltic upper oceanic crust: DSDP sites 417 and 418. In: Bebout, G.E., Scholl, S.W., Kirby, S.H., Platt, J.P. (Eds.), Subduction: Top to Bottom. American Geophysical Union, Washington, pp. 19–38.

Sun, S.S., McDonough, W.F., 1989. Chemical and isotopic systematics of oceanic basalts: implications for mantle composition and processes. Geol. Soc. London, Spec. Publ. 42, 313–345.

Taylor, S.R., McLennan, S.M., 1985. The Continental Crust: Its Composition and Evolution. Blackwell, Oxford, p. 312.

Terabayashi, M., Masada, Y., Ozawa, H., 2003. Archean ocean-floor metamorphism in the North Pole area, Pilbara Craton, Western Australia. Precambrian Res. 127, 167–180.

Tilley, D.B., Eggleton, R.A., 2005. Titanite low-temperature alteration and Ti mobility. Clays Clay Miner. 53 (1), 100–107.

Van Baalen, M.R., 1993. Titanium mobility in metamorphic systems: a review. Chem. Geol. 110, 233–249.

Van Hees, E.H.P., Shelton, K.L., McMenamy, T.A., Ross Jr., L.M., Cousens, B.L., Falck, M., Robb, M.E., Canam, T.W., 1999. Metasedimentary influence on metavolcanic-rock-hosted greenstone gold deposits: Geochemistry of the Giant mine, Yellowknife, Northwest Territories, Canada. Geology 27, 71–74.

Weiershäuser, L., Spooner, E.T.C., 2005. Seafloor hydrothermal fluids, Ben Nevis area, Abitibi greenstone belt; implications for Archean (approximately 2.7 Ga) seawater properties. Precambrian Res. 138, 89–123.

Winchester, J.A., Floyd, P.A., 1977. Geochemical discrimination of different magma series and their differentiation products using immobile elements. Chem. Geol. 20, 325–343.

Wood, S.A., 2005. The aqueous geochemistry of zirconium, hafnium, niobium and tantalum. In: Linnen, R.L., Samson, I.M. (Eds.). Rare-Element Geochemistry and Mineral Deposits. Geological Association of Canada, GAC Short Course Notes 17, 217–268.